Self-Similarity of Surface Wave Developments under Tropical Cyclones

Vladimir N. Kudryavtsev[1], Maria V. Yurovskaya[2], and Bertrand Chapron[3]

[1]Russian State Hydrometeorological University / Marine Hydrophysical Institute
[2]Marine Hydrophysical Institute
[3]IFREMER

November 21, 2022

Abstract

2D-parametric model is used to simulate waves under Tropical Cyclones (TCs). Set of equations describing either wind waves development and swell evolution, is solved using method of characteristics. Wave-rays patterns provide efficient visualization on how wave trains develop and travel through TC varying wind field and leave storm area as swell.

The superposition of wave-trains rays exhibits coherent spatial patterns of significant wave height, peak wavelength and direction, depending on TC characteristics, - maximal wind speed (um), radius (Rm), and translation velocity (V). Group velocity resonance leads to appearance of waves with abnormal energy between the TC right and front sectors, further outrunning as swell through the TC front sector. Yet, when TC translation velocity exceeds a threshold value, waves cannot reach group velocity resonance, and travelling backwards, form a wake of swell systems trailing the forward moving TC.

2D-parametric model solutions are parameterized using 2D self-similar universal functions. Comparisons between self-similar solutions and measurements, demonstrate excellent agreement to warrant their use for scientific and practical applications. Self-similar solutions provide immediate estimates of azimuthal-radial distributions of wave parameters under TCs, solely characterized by arbitrary sets of um, Rm and V conditions. Self-similar solutions clearly divide TCs between slow TCs fulfilling conditions Rm/Lcr>1, and fast TCs corresponding to Rm/Lcr <1, where Lcr is a critical fetch. The region around Rm/Lc = 1 corresponds to the group velocity resonance conditions, leading to the largest possible waves generated by a TC.

Self-Similarity of Surface Wave Developments under Tropical Cyclones

Vladimir Kudryavtsev (1,2), Maria Yurovskaya (2,1) and Bertrand Chapron (3,1)

(1) Russian State Hydrometeorological University, St. Petersburg, Russia,

(2) Marine Hydrophysical Institute, Sebastopol, Russia

(3) Laboratoire d'Oceanographie Physique et Spatiale, Ifremer, Plouzane, France,

Corresponding author:

Vladimir Kudryavtsev

e-mail: kudr@rshu.ru

Key points

1. Superposition of wave-trains rays provides efficient visualization on how waves develop under TC and leave it as swell.

2. Parametric model solutions are described using 2D self-similar universal functions.

3. Self-similar solutions demonstrate good agreement with measurements that warrant their scientific and practical applications.

ABSTRACT

2D-parametric model is used to simulate waves under Tropical Cyclones (TCs). Set of equations describing either wind waves development and swell evolution, is solved using method of characteristics. Wave-rays patterns provide efficient visualization on how wave trains develop and travel through TC varying wind field and leave storm area as swell.

The superposition of wave-trains rays exhibits coherent spatial patterns of significant wave height, peak wavelength and direction, depending on TC characteristics, - maximal wind speed (um), radius (Rm), and translation velocity (V). Group velocity resonance leads to appearance of waves with abnormal energy between the TC right and front sectors, further outrunning as swell through the TC front sector. Yet, when TC translation velocity exceeds a threshold value, waves cannot reach group velocity resonance, and travelling backwards, form a wake of swell systems trailing the forward moving TC.

2D-parametric model solutions are parameterized using 2D self-similar universal functions. Comparisons between self-similar solutions and measurements, demonstrate excellent agreement to warrant their use for scientific and practical applications. Self-similar solutions provide immediate estimates of azimuthal-radial distributions of wave parameters under TCs, solely characterized by arbitrary sets of um, Rm and V conditions. Self-similar solutions clearly divide TCs between slow TCs fulfilling conditions Rm/Lcr>1, and fast TCs corresponding to Rm/Lcr <1, where Lcr is a critical fetch. The region around Rm/Lc = 1 corresponds to the group velocity resonance conditions, leading to the largest possible waves generated by a TC.

Plain Language Summary

2D-parametric model is used to simulate waves under Tropical Cyclones (TCs). Solution of model equations using method of characteristics, provides distribution of wave energy, peak frequency and direction along wave-rays. Wave-rays patterns provide efficient visualization on how wave trains develop and travel through TC wind field and leave storm area as swell. Superposition of wave-rays exhibits coherent spatial patterns of wave parameters depending on TC characteristics, - maximal wind speed (um), radius (Rm), and translation velocity (V). The most striking feature of wave fields under TC is the azimuthal asymmetry, resulting from group velocity resonance between waves and moving TC. This effect leads to appearance of waves with abnormal energy between the TC right and front sectors, further outrunning as swell in TC heading direction. 2D-parametric model solutions are parameterized using 2D self-similar universal functions. Comparisons between self-similar solutions and measurements, demonstrate excellent agreement. Self-similar solutions provide immediate estimates of azimuthal-radial distributions of wave parameters under TCs. Suggested self-similar solutions can be used for scientific and practical applications, in particular to provide fast estimates of waves generated by moving TC with arbitrary sets of um, Rm and V.

1. Introduction

Besides strong interests for marine engineering and navigation safety, tropical cyclone (TC)–generated wave fields are now systematically invoked as essential components of the two-way, air–ocean coupled system to control the dynamical evolution of extreme events. Marine-atmosphere extremes are also crucial for the determination of coastal sea levels and coastal erosion.

In that context, there have been considerable efforts to improve knowledge about the main characteristics of TC–generated surface waves, both from measurements and numerical modeling experiments. Full sophisticated spectral wave models certainly have the capability to provide detailed wave information [e.g. Moon et al., 2003, Liu et al., 2017, Julien et al., 2020]. Yet, computer limitations, lack of precise well-resolved surface winds and/or needs to consider large ensembles of solutions, especially to help forecast TC dynamics, also invite to develop more simplified but robust solutions.

For instance, a practical model should help to rapidly anticipate and document the role of partial resonance effects to increase the effective fetch and duration of the wave-growth process in the different directions of tropical weather systems, i.e. the wave trapping phenomenon [e.g., King and Shemdin, 1978; Dysthe and Harbitz, 1987; Young, 1988; Bowyer and MacAfee, 2005; Young and Vinoth, 2013; Kudryavtsev et al., 2015]. To further note, severe weather systems are difficult to fully characterize, making remote sensing techniques essential for observing surface processes. At time, satellite observations can produce spatially well-resolved snapshots of surface winds [e.g. Mouche et al., 2019, Combot et al., 2020]. However, most extreme events may still be under sampled, and this lack of observations cannot always lead to fully characterize spatio-temporal surface wind forcing conditions. These wind forcing uncertainties may then cause large biases for surface momentum fluxes and wave developments.

Nevertheless, despite this expected spatio-temporal complexity of extreme weather systems, generated surface waves are generally reported to well follow self-similar fetch laws, originally suggested by Kitaigorodskii [1962]. For very intense low pressure systems, the main vortex structure of the winds and the motion of this vortex apparently solely govern the spatial distribution of generated waves and their associated directional characteristics (energy, wavelength). Thus, the wave field largely mirrors the main overall vortex structure of the winds,

but wave developments can become strongly asymmetrical, from the wave trapping phenomenon, due to the translating motion of the main vortex.

From experimental campaigns, airborne scanning radar altimeter measurements, first reported by Wright et al. [2001] and Walsh et al. [2002], largely support this assumption. These airborne measurements have been more recently analyzed [Hwang et al., 2017, Hwang and Walsh, 2018], and provide unique quantitative information about the azimuthal and radial distributions of wave spectra inside TCs. In the front half of a TC, single wave systems seem to largely dominate. In the other TC sectors, multiple wave systems are generally observed, in the back and right quarters outside the radius of maximum wind.

In this paper, a first objective is thus to apply the revised 2D-parametric model [Kudryavtsev et al., companion paper] to predict wave field developments under moving TCs, and to assess how these predictions are consistent with available airborne and satellite observations. Moreover, a second objective is to demonstrate how these proposed 2D-parametric model predictions can be analytically reduced using 2D self-similar functions. Considering a prescribed structure of the TC winds and its translation, this is successfully performed. The reduced self-similar solutions shall then be considered as the generalization of 1D fetch-laws for TC-generated waves, to provide useful robust first guess estimates for practical nowcasting and scientific applications.

The approach is outlined, section 2, with solutions for stationary TCs presented in section 3, and for moving TCs in section 4. Analysis are then performed, and reported in section 5, including comparisons with available airborne and satellite observations. In section 6, self-similarity properties of the numerical outputs are demonstrated, and practical solutions are proposed. Following a short discussion, section 7, concluding remarks are givenin section 8.

2. Approach

The governing model relationships are represented by a system of equations, Eq. (47) to (50), in [Kudryavtsev et al., companion paper, hereinafter referred as Part1]. The model is written in characteristic form, and describes the along-ray evolution of energy, frequency and direction of wave trains travelling under the forcing of a wind field varying in space and time.

2.1. Wind field

To model the radial wind speed profile, the form suggested by Holland [1980] is adopted:

$$u(r) = \left[\left(u_m^2 + u_m rf \right) \left(\frac{R_m}{r} \right)^B \exp\left(-\left(\frac{R_m}{r} \right)^B + 1 \right) + \left(\frac{rf}{2} \right)^2 \right]^{1/2} - \frac{rf}{2} \qquad (1)$$

which is widely used to simulate TC wind field. In (1), u_m is the maximum wind speed at 10-meter level, R_m is the radius of maximum wind speed, r is radial distance, B is the shape parameter. In addition, the wind velocity is considered to spiral towards the TC eye, with a mean inflow angle $\varphi_{in} = 20^0$ [Zhang and Uhlhorn, 2012]. In the following calculations, the shape-parameter B in (1) is set to $B = 1.5$. TC wind field (1) can be either stationary or moving with translation velocity, V, directed along the y-axis. Such wind field is considered as input parameter to solve the system of equations (47) to (50) from Part1.

2.2. Initialization

Hereinafter, the problem is solved by the method of characteristics, stated in a coordinate system moving with the TC, where the coordinate origin coincides with the TC eye. In this case, TC translation velocity, V, must be added to the r.h.s. of the wave train trajectories, eq. (50) in Part 1.

Each of the characteristics represents a wave-ray along which a wave train can develop, starting from its initial instant of generation. From a set of N wave trains, the starting point of the j-th wave train at initial time $t = 0$ is $(x^j, y^j) = (x_0^j, y_0^j)$. For initial conditions for each ray, we define the peak frequency, ω_{p0}^j, and energy, e_0^j, through their duration-development laws $\omega_p u / g = c_{\alpha_t} \left(tg / u \right)^{q_t}$ and $eg^2 / u^4 = c_{e_t} \left(tg / u \right)^{p_t}$ correspondingly, with the wave direction aligned with the local wind $u(x_0^j, y_0^j)$. Initial values follow from a «small» initial time-interval τ:

$$\begin{aligned} \omega_{p0}^j &= c_{\alpha_t} \left[g / u(x_0^j, y_0^j) \right] \tau^{q_t} \\ e_0^j &= c_{e_t} \left[u^4(x_0^j, y_0^j) / g^2 \right] \tau^{p_t} \end{aligned} \qquad (2)$$

where c_{α_t}, c_{e_t}, q_t, and p_t are duration-laws constants. These constants are not free, but are unambiguously linked to the corresponding fetch-laws constants c_α, c_e, q, and p [see e.g. Kudryavtsev et al., 2015; Dulov et al., 2020 and references cited therein]:

$$\begin{aligned} q_t &= q / (1 + q), \quad p_t = p / (1 + q) \\ c_{\alpha_t} &= c_\alpha \left[(1 + q) / (2 c_\alpha) \right]^{q_t}, \quad c_{e_t} = c_e \left[(1 + q) / (2 c_\alpha) \right]^{p_t} \end{aligned} \qquad (3)$$

In the following calculations, the initial time-interval is assigned as $\tau = 5$ min, and the reference time is counted from τ.

The wave-trains with initial parameters (2) are "seeded" on a polar grid shown in Fig.1. By default, the grid azimuthal resolution is $\Delta\varphi = 9^0$ with radial logarithm-spacing $\Delta r/r = \Delta\varphi$ and minimal r_{min} equal to $r_{min} = R_m/4$, R_m is radius of maximum wind speed.

The system of differential equations, written in characteristic form, is solved numerically using the Runge-Kutta method of the 4-th order. To accelerate calculations, we used variable time-step for integration, increasing as time squared, but not exceeding 30 min.

Figure 1 is about here

Throughout the paper the following notations/definitions are used : TC moves in direction of y-axis, azimuth $\varphi = 0^0$ corresponds to TC heading, azimuthal directions are counted counter-clockwise. To describe the wave field development, TC areas are divided between Right-, Left-, Front- and Back-Sectors, R-S, L-S, F-S, and B-S, correspondingly, as indicated in Fig.1. In the R-S and L-S, wind velocity is almost aligned or opposite to the TC heading, respectively. In the F-S and B-S, wind is directed almost across the TC heading. Each of these sectors can additionally be divided in half, forming eight slices with azimuthal step 45 deg.

3. Stationary TC
3.1. Dynamics of Individual Rays

The dynamics of four wave trains are first considered, starting at radial distances: $r = R_m/2$ $r = R_m$, $r = 2R_m$, and $r = 4R_m$ for a TC maximum wind speed $u_m = 50$ m/s and $R_m = 50$ km, Fig.2. On the initial stage, traveling through the complex wind velocity field varying both in speed and in direction, wave trains exhibit fast development, i.e. rapid growth of significant wave height (SWH) and the associated peak wavelength. At the beginning, developing waves follow the veering wind direction, but in the course of their development, waves become too "inertial", start to deviate from the wind direction, and travel outwards the TC. The wave trains attain maximal energy, with monotonically growing wavelength, at radial distance around R_m. Then, due to deviation from wind direction and a decrease of the wind speed at $r > R_m$, wave breaking dissipates the energy, and the energy balance adjusts to the reduced forcing. Further, passing the point of a local full development, i.e. $\alpha = u_{10}\cos(\varphi_p - \varphi_w)/c_p \approx 0.85$, the wind energy input terminates, and wave trains travel outwards as swell systems.

Solid and dash lines in Fig.2 demonstrate the model simulations with and without accounting for the wave focusing effects, described by the 1st term in r.h.s of Eq. (47) in Part 1. For the azimuthally isotropic wind field with radial profile (1), the gradient of wind direction, G_W, is directed along the tangent to the circle and has the magnitude $|G_W| = 1/r$. During the initial stage, growing waves develop along the wind direction. Hence, the projection of G_W on direction perpendicular to the wave direction, $G_W^n = -|G_W| \sin \varphi_{in}$, is negative. It leads to the focusing of wave-rays, acting as extra energy input source to wind waves. For the train started in vicinity of the eye, the effect of the ray focusing results in the appearance of a caustic zone (identifying as sharp minimum of black line in the upper-right plot, Fig. 2) on the initial stage of development. However, referring to Fig.2, the focusing effect results in an overall negligible impact on the energy and peak wavelength while wave trains are subject to intense wind forcing. The reason is that the rate of the energy input through focusing is much smaller than the rate of the energy gain from the wind and wave breaking dissipation. Moreover, the dissipation is a strongly non-linear function of wave steepness, providing a threshold-like energy level limitation to any small disturbances acting on the energy balance. On the contrary, when wave trains turn into regime of swell systems, focusing effects can become very effective and result in remarkable wave energy enhancement in the pre-caustic zone (identifying as sharp maximum of blue line in the upper-right plot) and, subsequent wave energy attenuation away from the caustic zone, Fig.2.

3.2. Rays Superposition

Superposition of wave-rays, seeded from the polar grid, Fig.1, is shown Fig.3. To plot the composition of a large number of rays, an overlapping "rule" applies, i.e. the ray with the largest local wavelength is on top of all others. These longest waves are associated with the most developed ones, and this representation emphasizes primary wave systems.

The spatial distribution of wave-train parameters then exhibits an apparent azimuthal isotropy. In this specific case, the maximum of energy locates at radial distance close to R_m (Fig.3, upper-left). Once wave trains become locally fully developed, they further travel outwards as swell systems, almost in radial direction. For these emerging swells, energy decreases, but the wavelength is conserved (Fig.3, upper-right and upper-left).

Wave direction departures from the wind ones results in important feature, namely the development of wave field from the TC center towards its periphery. A map of wave-train travel time, Fig.3, down-left, clearly demonstrates that local time for the most developed waves to appear, increases from the TC eye towards its periphery. Accordingly, the vicinity of the TC eye can be considered as the area where a primary wave system started. Moreover, for the given time, t, a radial contour, $r_d(t)$, can correspond to a boundary dividing wave fields between its stationary part, $r < r_d(t)$, where waves exhibit features typical to (stationary) fetch-limited development, and its evolving part, $r > r_d(t)$, where waves develop in time with properties typical for duration-limited development. In 1D-case, such a division of a wave field between two regions exhibiting fetch- and duration-limited development was introduced by Kitaigorodskii [1962] for the evolution of wind waves from the coast starting from the state of the rest.

4. Moving TC

4.1 Rays patterns.

Wave train dynamics, starting on radial distances $[R_m/2, R_m, 2R_m, 4R_m]$ with azimuthal step 30deg for a TC with u_m =50m/s and R_m =50 km, moving with different translation velocities V = [0, 5, 7, 12] m/s are displayed Fig.4.

As compared to a stationary TC (upper row in Fig.4), TC motions induce radical changes for the trajectories and distribution of wave parameters. TC motions introduce marked azimuthal anisotropy, increasing for faster TCs. Similar to the stationary TC case, generated waves at initial stage follow the veering wind, but associated to the TC translation, developing and relatively slow wave-trains can travel backwards. Most distinct wind directions relative to the TC translation velocity, V, in the Right- and Left-Sectors (R-S and L-S), results in the appearance of important azimuthal anisotropy for the patterns of wave-rays.

Figure 4 is about here

Qualitatively, kinematics of the train can be described as the following. All wave-trains starting in the F-S, L-S and in the left half (slice) of B-S, travel backwards with some adjustment to the veering wind, then "detach" from the wind forcing, and leave the TC area as swell systems. Due to the TC motion, the residence time of these trains is reduced compared to the stationary case, and therefore they are less developed.

Kinematics for wave trains starting in the R-S and in the right slice of B-S is more complicated. First, we consider TC cases with V =5m/s and V =7m/s, Fig.4. Except for the trains starting at

$r < R_m$ in the upper slice of R-S, other trains, being initially slow, first travel backwards. In the course of the wave development, the group velocity can equalize the TC translation velocity. At these points, trajectories are largely inflected and take a « hook »-like shape. Trough of this hook-like trajectory corresponds to the turning point, where the direction of the wave-trains changes from backward to forward relative to the TC motion. Following (Dysthe and Harbitz, 1987), we term this effect as local group velocity quasi-resonance between wave and TC motion. Passing the turning point, these quasi-resonant trains move forward, slowly relative to the TC. Therefore, their residence time under TC forcing is significantly increased. Within the TC R-S, the waves gain energy from the wind, rapidly develop, travelling through F-S in TC heading direction. These trains are the most developed, and their energy and wavelength significantly exceed the corresponding values for the stationary TC case.

Note, wave trains starting at $r < R_m$ in the upper slice of R-S, travel backwards through the complex wind field, with decreasing speed and rotating direction. As a consequence, these trains being strongly undeveloped enter the TC L-S as swell waves, with direction opposite to the local wind, Fig.4.

For large TC translation velocity, case $V = 12$m/s in Fig.4, none of the wave trains starting in the right-half of the TC are capable to reach the group velocity resonance. Following a 1D parametric model [Kudryavtsev et al., 2015], wave-trains can reach the group velocity resonance, only if the TC maximal wind speed (u_m), radius of u_m (R_m), and translation velocity (V), satisfy the condition

$$\sqrt{2}\, gR_m / u_m^2 > c_T \left(u_m / V \right)^{1/q} \tag{4}$$

with $c_T = 6.5 \times 10^4$ and $q = -0.275$, parameters used by Kudryavtsev et al. (2015). For the Fig.4 cases, TC R_m=50km and u_m=50m/s, the maximal V satisfying inequality (4) is $V = 10$m/s. Case $V = 12$m/s thus does not satisfy this condition (4), and hence can be treated as wave generation by fast TC. In this case, the group velocity of all developing waves are always less than the TC translation velocity, and waves are all traveling backwards and leave the storm area.

Figure 4 is about here

4.2. Time evolution of wave parameters along ray

Fig.5 illustrates the time-evolution of wave parameters along the trajectories of four wave trains selected from Fig.4. Three of these trains (marked by red, blue and green in Fig.5) satisfy conditions of the group velocity resonance. Two out of these three (red and blue) represent

"family" of trains starting in the TC R-S, in the area of maximum wind. Travelling with the TC under maximal wind forcing, these wave trains rapidly develop, attaining the maximum of their energy, Fig.5. Further, these wave trains move over areas of decreasing wind speed. Their energies start to decrease, due to the impact of unbalanced wave breaking dissipation appearing after the reduced wind forcing. With the continuing decrease of wind speed and rotation of its direction, the inverse wave age, $\alpha = u_{10}\cos(\varphi_p - \varphi_w)/c_p$, becomes less than 0.85, in about 7 hours after initial generation. Wave trains turn into a swell regime outrunning the TC.

The other train (green in Fig.5) represents a "family" of resonant wave trains initially generated at the periphery of TC R-S. In the course of their development, before and after the turning point, the wave trains travel through increasing wind forcing conditions. Entering the area of highest wind speed, these wave trains equalize their group velocities with V, and the ray becomes perpendicular to the TC heading, Fig.5. Now traveling with the TC, waves gain energy in the area of maximal wind, and then turn into swell regime with the rotation and decrease of local winds.

Both families of these resonant wave trains represent the longest and the highest waves generated by the TC. However, the family initially generated at the periphery, shall attain a maximal development after a significantly longer time-integration than those starting in the maximal wind speed area: 6-7 hours against 17 hours in specific case shown Fig.5.

Solid and dash lines in Fig.5 demonstrate the model simulations with and without accounting for the wave focusing effects. From simulations, during the development stage, the rate of energy input through focusing is much smaller than from the wind forcing. Hence, effect of the focusing is negligible on wave train dynamics. However, when wave trains attain a swell regime, waves travel as free waves, and focusing effects result in local wave energy enhancements in the pre-caustic zone, e.g. corresponding to a local peak in the cross-ray divergence factor shown in the upper-right plot of Fig.5. Subsequent wave energy attenuation follows away from the caustic zone due to wave-rays defocusing, Fig.5.

Figure 5 is about here

4.3. Superposition of all wave trains.

Hereafter, we consider wave field parameters resulting from the superposition of all wave-trains originating from the polar grid points shown in Fig.1. As mentioned in sec.3.2, an "overlapping rule" applies to plot the composition of the large number of the rays, i.e. the ray with the largest local wavelength is traced on top of other. The longest wave is associated with the most developed one. Therefore, such representation emphasizes the primary wave system.

4.3.1. Time development

Overlapping large number of rays provides a clear presentation on the space-time evolution of wave parameters under TC forcing, Fig.6. On the initial stage, t=5h, a circular pattern of the most developed waves appear in the vicinity of the maximum wind speed, which is however shifted backwards due to the TC displacement. Even at this initial stage, asymmetries in both wavelength and significant wave height (SWH) of waves developing in the left- and right-half of TC are already well expressed. As discussed, asymmetries appear with the alignment of the group velocity of wave-trains and TC heading in the right-half, and their opposite direction in the left-half. This impacts, the residence time of wave-trains in the high wind speed area and the consequent wind energy gain.

At larger time, t=10h and more, Fig.6, wave-trains subject to group velocity resonance, move forward. Being slow relative to TC, they rapidly develop, gaining energy from the wind. A wave front is well detectable where the most developed waves advance, Fig.6. The wave front corresponds to a line connecting points with abrupt changes of both wavelength and SWH along the rays. Note, this advancing front of "the most developed" waves extends towards the TC periphery and overlaps the area with developing wind wave trains, forming mixed sea areas. Referring to Fig.6, one may find that in 20 hours, waves generated from the TC high-wind area cover a total area with radius $5R_m$. For this particular case, this time of development can be considered as the time-scale the wave field reaches stationarity.

4.3.2. "Stationary" fields

Fields of wave parameters (energy, wavelength and direction) generated by a TC with the same characteristics, u_m=50m/s and R_m=50km as in Fig.6, but with different translation velocities $V =$ [3, 5, 7, 12] m/s, after a large integration time, 40 hours, are shown in Fig.7. After 40 hours, all wave trains can outrun the TC area of influence. Therefore, following the "overlapping rule", wave fields, Fig.7, correspond to the most developed wave trains at any given spatial point, i.e. can be treated as stationary solutions for the primary wave system generated by the TC.

The superposition of large number of rays provides spatial patterns of wave parameters already discussed. In particular, except for the fast TC, case $V =$12m/s in Fig.7, the effect of the group velocity resonance results in strong azimuthal asymmetry with maximal values of energy in the

area of maximum wind speed, around a region dividing the TC between the F-S and R-S sectors, with the longest waves emitted through F-S in the TC heading direction. The faster the TC, the larger are both the SWH and length of TC-generated waves. This applies as long as the TC translation velocity does not exceed a "threshold" value. For such conditions, waves generated inside a very fast TC never reach the group velocity resonance. All the developing waves travel backwards, forming a wake of swell systems behind the TC, illustrated for V =12m/s in Fig.7.

A mosaic of wave parameters generated by TCs with V =8m/s, R_m =[30 50 70] km and u_m = [30 50 70] m/s is shown Fig.8. Together with Fig.7, Fig. 8 demonstrates large variability of SWH and peak wavelength fields, both in magnitudes and shape of the resulting patterns, depending on the TC parameters. However, a careful inspection of Fig.7 and Fig.8, reveals very similar spatial distributions of H_s, λ_p and φ_p for some particular combinations of TC parameters [V, R_m, u_m], e. g., the field of wave parameters for a TC set [8, 30, 30] in Fig.8 and the predicted field for a TC set [5, 50, 50] in Fig.7, or wave fields for TC sets [8 30 70] and [8 70 50] in Fig.8. Such a property of TC-generated wave fields will further be considered in details in Sec.6.

Figure 8 is about here

5. Wave Systems

5.1. Decomposition on wind waves and swell systems

Wave parameters shown in Fig.7 and Fig.8, correspond to the primary, the most developed, wave system. Other coincident rays are beneath. Fig.9 shows all wave trains and distributions of corresponding parameters passing through a fixed box, indicated in Fig.7, during the 40 hours interval.

Figure 10 is about here

First, referring to Fig.9-left, a rather large number of wave-trains are predicted, traveling in different directions, with various energies. Some of these wave trains, with minimal SWH, originate from the box, to leave it in the course of their development. Distributions of SWH and traveling time of these trains over wavelength and directions are shown, Fig. 9-mid and -right, correspondingly. Two wave systems can be revealed. The first system is associated to wind waves with directions coinciding with the wind direction. This system thus includes all wind waves captured within this box, either originating inside or outside the box.

The second type of the waves, waves with wavelengths around 350-400m and directions deviating from the wind, can be classified as swell waves. These waves can reach large SWH values (from 10m to 15m) with directions to the left from the TC heading.

A careful inspection of the travel-time-histogram further helps to divide these swell wave-trains on two sub-systems: a first one corresponding to «small» travel time, about 10 to 15 hours, with the largest SWH, about 15m, and a second one corresponding to "long" integration time, 50-65 hours, with smaller SWH, about 10m. Both swell sub-systems result from group-velocity resonance. However, the fore-running swell originates from wind waves generated within the high wind area, around a region bounded between R-S and B-S. The other swell system originates from wind waves generated in the periphery (see Fig.4 and Fig.5). Both swell systems can exist independently, possibly leading to superpositions of waves with very large amplitudes. Still, superpositions may only appear after a rather long time interval, about 50 hours and more, predefined by the travel time of the swell originating from the TC periphery.

The whole ensemble of wave-trains, falling into each of the boxes spread over TC as shown in Fig.1, are then further divided in two wave systems: (i) "wind waves", with local inverse wave age $\alpha_p \equiv \cos(\varphi_p - \varphi_w)u(x, y)/c_p \geq 0.85$, and "swell", with local inverse wave age $\alpha_p < 0.85$. Then, among all these wave trains classified as "wind-waves" or "swell" in a given box, two wave trains are selected, having the largest wavelength among all waves belonging to each of the two system classes. This provides the spatial distribution of wave parameters for both types of wave systems under a TC. An example of TC-generated wave fields (shown before, Fig.7) is displayed Fig.10.

Figure 10 is about here

Wind-waves fields clearly exhibit a left-to-right asymmetry, associated to the difference between wind and TC heading directions. An alignment between wind and TC heading, in the R-S, leads to an increased residence time of waves within the storm area, and hence to the stronger development. Referring to Fig.10, cases V = [3, 5, 7] m/s, waves starting around R_m, at the boundary between R-S and B-S, subject to the group velocity resonance, can lead to the formation of an area of maximal energy. This zone corresponds to pure wind seas, and does not contain swell system (compare plots for wind waves and swell system). Still, the direction of this system of wind-waves does not align with the local wind direction. This system thus overlaps younger wind waves, aligned with the local wind, that start at the TC periphery and travel backwards when crossing the area of maximal energy. These young waves represent a secondary system of local wind-waves, distinct from well-developed wave system.

Wind-wave trains with maximal energy entering a veering wind area, turn into the regime of swell system, compare 3rd and 4th rows in Fig.10. This swell system is the longest one, and start to spread ahead of the TC; its energy attenuate with increasing distance due to dissipation and effect of group defocusing effect, 2nd row in Fig.10. Swell emerging from wind waves developing in other parts of the storm, finally cover the whole TC area and travel under different directions compared to the wind. Except over the area of maximal energy, where pure wind waves propagate, wave field in the other parts of TC is composed by two main systems, swell and wind waves.

For a fast TC, $V =$12m/s in Fig.10, group velocity resonance is not possible and all developing wind-wave trains travel backward. Still, the increased residence time results in a marked left-to-right TC asymmetry, expressed as regions of high wave energy on the boundary between R-S and B-S. In this case of a fast TC, most of the TC storm area is covered by pure wind waves, and swell can only appear in its rear part, when developing wind waves travel backwards through the decreasing and veering wind area.

5.2 Comparison with observations

Model simulations are compared with some reported observations, to assess the model capability to quantitatively reproduce general features of observed wave fields under TC.

5.2.1   Spectral distributions over TC

Hwang and Walsh [2018] reappraised airborne 2D wave spectral measurements inside TCs. These measurements provided great opportunity to investigate evolution of the waves and their spectral content in different parts of TCs. Fig. 11 displays 2D wave spectra [Hwang and Walsh, 2018, their Fig 4], inside TC Ivan for 8 azimuthal slices with width pi/4 counterclockwise from TC heading, at radial distances from 50 to100 km and from 150 to 200 km.

Fig.11 is about here

Model distributions (histograms) of the wave-trains energy over the wavelength and direction in the same TC slices are also shown in Fig.12. These model distributions (histograms) serve as proxies of the observed spectra. Model spectra in Fig.11 correspond to TC with parameters: $u_m =$ 50m/s, $R_m =$ 50km, and $V = $ 5m/s, close to TC Ivan characteristics. The azimuthally isotropic model wind field with the radial profile (1) differs from the real one. However, this difference is acceptable, assuming that it is sufficient to test the model capabilities on a quantitative level.

From careful inspection, Fig.11, the model "spectra" are comparable with observations in both the area of high winds and on the TC periphery, from 150 to 200 km. The model well reproduces SWH, directions and wavelengths of the primary wave system in different parts of TC. Similar to observations: (i) directionally monomodal spectra are dominant in slices 1, 7, and 8 of the TC coverage area; (ii) overall, there is a leftward and frontward trend of wave propagation inside the TC coverage area, except for slices 3 and 4 where waves propagate backward; (iii) the highest waves are in the front sectors, slices 1, 8, and 7; (iv) wave energy in the back sectors is significantly reduced; (v) "spectra" patterns in the area around R_m are very similarly to those outside the R_m.

Although, the model simulations were performed using an idealized wind field described noticeably different from the one presented by Hwang and Walsh [2018], this quantitative agreement is encouraging.

An other example of the comparison is the directional buoys wave data on Australia's North-West shelf during the passage of 9 TC in 1995-2000, reported by Young [2006]. A typical wave directional spreading functions measured in each of the four quadrants of TC are shown in Fig. 12, right-half (taken from Young [2006] his Fig.5). Positions of the measurements are shown in the right column in Fig.12. The measurements revealed that the directional spectra gradually skew from the dominant wave direction towards wind direction. Plausible points of the dominant waves generation, obtained by backward ray tracing, are shown in the right column by the bullet points.

The left-half of Fig. 12 demonstrate model simulations stylized to Young's [2006] data shown in the right-half. Model TC parameters are R_m=50 km, u_m = 50 m/s and V =7 m/s. Histograms of SWH of trains passing a square with the side of $r/3$ are considered as a proxy of wave spectra (see sec. 5.1) and shown in left column of Fig.12. Locations of the squares centers are indicated in the right column of Fig.12, left-half. Angular-frequency distributions of SWH in the wave-trains histograms (spectra) are in a quantitative agreement with the measurements, reproducing correctly azimuthal location of dominant swell relative to the wind direction.

The right column in the left-half of Fig.12 demonstrate initial position (starting point) and trajectory of the dominant waves (observed in the "point of measurements") in moving (red lines) and stationary (green lines) coordinate systems. Model staring positions of waves are in conformity with Young' [2006] estimates, i.e. compare right columns in the left-side and right-half of Fig.12. Notice, that length of the trajectories in stationary coordinate system "correlates"

with corresponding SWH, to justify the application of self-similarity laws for wave development with use of the extended fetch approach. This is discussed in details in the following Sec.6.

5.2.2. Significand wave height profiles across TC

Satellite altimeter measurements can provide unique data on spatial distributions of wave heights inside TC [Quilfen et al., 2006; Quilfen et al., 2010; Kudryavtsev et al., 2015]. Zhang and Oey [2019] presented 24 years of TC SWH measurements in the western North Pacific to investigate the dependence of generated waves on TC translation velocity and intensity. According to [Zhang and Oey, 2019], for slow TC, V <3m/s, the SWH distribution is almost symmetrical over the TC area. But for TC cases with larger translation velocity, V from 3m/s to7m/s, a strong SWH asymmetry arises in the right-front sector, exceeding 7–8 m and reported to attain 10-11 m at u_m = 50 m/s. These values are averaged over a large ensemble of TCs, and for each specific case, SWH measurements can largely differ.

Fig.13 is about here

Profiles of the wave energy along the altimeter tracks crossing TC Isabel and Songda close to their eyes, already analyzed in Kudryavtsev et al. [2015], are shown Fig.13. These cases correspond to strong asymmetries of wave energy between TC right- and left- sectors.

To simulate the observations, wind profiles are specified using (1) with u_m =70m/s, R_m =30km, shape parameter B =1.5, and translation velocity V = 6m/s, closed to the TCs parameters [see Table 1 from Kudryavtsev et al., 2015]. Fields of the wavelength and SWH parameters for the primary wave system, and their profiles along the altimeter tracks are displayed in Fig.13. Predicted wave energy profiles are consistent with altimeter observations for both TCs. The model reproduces the left-to-right TC asymmetry, with the energy of the waves in the right TC sector attaining 16m^2, in agreement with satellite measurements. Some deviations between predicted and measured energy appear in left sector at large distance, r/R_m between 4 and 10, likely related to differences between the idealized and real wind profiles.

6. On Self-similarity of TC 2D wave field
6.1. Approach

The revised 2D parametric model is thus capable to reproduce observed wave fields under TC extreme forcing conditions, and can thus be considered as a separate robust tool for wave investigations. To recall, this 2D model follows self-similarity concept. Therefore, the spatial

distribution of wave characteristics can also be anticipated to be self-similar, using proper scaling involving the main TC parameters: R_m, u_m, and V.

Classical self-similarity theory of wave growth in terms of 1D fetch-law has already demonstrated its efficiency to describe TC-generated waves using the equivalent fetch concept, X_{eq}, e.g., [Bowyer and MacAfee, 2005; Young 2017, and references herein). This equivalent fetch, termed also as effective fetch or trapped fetch, for moving TC is not only function of R_m, but also depends on V and u_m. Once X_{eq} is specified, expected maximal values of SWH in TC, $H_s^{\max}$, can then be found from the fetch laws (see e.g. review by Young [2017]).

Considering an idealized 1D model of wave development in the R-S and L-S, Kudryavtsev et al. [2015] further showed that the dimensionless energy, $\tilde{e}$, and peak frequency, α_p, of wind waves generated by moving storm at radius r, are indeed universal functions depending on the parameter r/L_{cr}

$$
\begin{aligned}
\alpha_p / \alpha_{p0} &= \varphi_\alpha \left(\tilde{r} / \tilde{L}_{cr} \right), \\
\tilde{e} / \tilde{e}_0 &= \varphi_e \left(\tilde{r} / \tilde{L}_{cr} \right),
\end{aligned}
\tag{5}
$$

where $\alpha_{p0} \propto \tilde{r}^q$ and $\tilde{e}_0 \propto \tilde{r}^p$ are the reference inverse wave age and energy for a stationary TC, corresponding to the standard fetch laws, with radius as fetch, scaled with g and local wind speed $u_r \equiv u(r)$; φ_a and φ_e are universal functions, and $\tilde{L}_{cr}$ is a critical fetch

$$
\tilde{L}_{cr} = c_{cr} \left(u_r / 2V \right)^{1/q}
\tag{6}
$$

defining a distance from the initial point of generation to the turning point where the group velocity of a developing wave train matches the TC translation velocity. In (6) c_{cr} is a constant linked to the fetch law exponent q and constant c_α is defined as: $c_{cr} = -c_\alpha^{-1/q} q / (1+q)$. For $\tilde{L}_{cr} < \tilde{r}$, wave group velocity resonance can occur in the right sector of a TC, while for, $\tilde{L}_{cr} > \tilde{r}$, the resonance condition cannot be fulfilled, and a developing wave train travels backward, leaving the TC right sector via its rear boundary. Within this 1D model framework, the self-similar relationships (5) are also valid in the left sector. The universal functions φ_a and φ_e are different, and wind waves travel and leave the left sector via the rear boundary.

Following this approach, we can check whether self-similar relationships of the kind (6.1) can be refined for a 2D TC wind field. To that end, 2D self-similar solutions are anticipated to take the following form

$$
\begin{aligned}
e/e_0 &= \Phi_e\left(r/L_{cr}, \theta\right), \\
\lambda_p/\lambda_{p0} &= \Phi_\lambda\left(r/L_{cr}, \theta\right), \\
\varphi_p - \varphi_{p0} &= \Phi_\varphi\left(r/L_{cr}, \theta\right),
\end{aligned}
\tag{7}
$$

where λ_{p0}, e_0, and φ_{p0} are reference distributions associated with azimuthally isotropic wave development under stationary TC, θ is azimuth, and Φ_λ, Φ_e and Φ_φ are 2D dimensionless functions accounting for the TC motion, $L_{cr} = \left(u_r^2/g\right)\tilde{L}_{cr}$ is dimension critical fetch (6). These dimensionless functions should take into account both the TC radius scaled by (6) and the azimuth. To search for solutions (7), model simulations are considered for a number of TCs with different parameters varying as: u_m =[30 50 70] m/s, R_m =[30 50 70] km, and V =[3, 5, 7, 8, 9, 10, 12] m/s. In total 3x3x7=63 model outputs were considered. But, the reference self-similar solutions must first be obtained for stationary TC, providing λ_{p0} and e_0 in (7).

6.2. Stationary TC: fetch-law scaling

An ensemble of 2D fields of wave parameters has been composed using 9 model simulations for stationary TC with u_m = [30, 50, 70] m/s, and R_m = [30, 50. 70] km. For each of these TC conditions, all wave trains passing through each of the predefined boxes, indicated in Fig.1, are accumulated. Among these wave trains in a given box, the longest wavelength is selected, and further considered as a proxy of the stationary primary wave system at a given spatial point.

Fig.14 displays azimuthally averaged radial distributions of SWH, the spectral peak wavelength and direction relative to the wind for the 9 TCs, represented in dimensionless form, associated with the fetch laws, as:

$$
\begin{aligned}
\tilde{H}_{s0} &= \tilde{R}_m^{p/2} f_h(\rho, \tilde{R}_m) \\
\tilde{\lambda}_{p0} &= \tilde{R}_m^{-2q} f_\lambda(\rho, \tilde{R}_m) \\
\varphi_{p0} - \varphi_w &= f_\varphi(\rho, \tilde{R}_m)
\end{aligned}
\tag{8}
$$

where $\tilde{H}_{s0} = H_{s0}g/u_m^2$, $\tilde{\lambda}_{p0} = \lambda_{p0}g/u_m^2$, $\tilde{R}_m = R_m g/u_m^2$, and subscript '0' denotes hereinafter the quantities related to stationary TC. In (8) $p = 3/4$ and $q = -1/4$ are the fetch law exponents,

and f_y with corresponding subscript $y = [h, \lambda, \varphi]$ is dimensionless function of $\rho = r/R_m$ and $\tilde{R}_m$.

As scaled, wave parameter profiles all collapse at radial distances about $r/R_m < 2$, where waves are young and developing, to then scatter for larger distances. To specify the dimensionless functions in (8), we introduce a radial distance, $r = r_0$, where wind waves turn into a swell regime. In general, r_0 scaled by R_m should be a function of $\tilde{R}_m$: $r_0/R_m = \rho_0(\tilde{R}_m)$. Where waves are under wind forcing, $\rho < \rho_0(\tilde{R}_m)$, dimensionless functions in (6.4) are empirically specified as

$$
\begin{aligned}
f_h^w(\rho) &= 5.6 \times 10^{-3} \tanh\left[2(\rho - 0.25)\right]\left[1 - 0.1(\rho - 0.25)\right] \\
f_\lambda^w(\rho) &= 6.8 \times 10^{-2} m_\lambda \tanh\left[1.5(\rho - 0.25)\right] \\
f_\varphi^w(\rho) &= -\left(\pi/3\right)\tanh(0.9\rho)
\end{aligned}
\tag{9}
$$

where superscript 'w' in f_y denotes regime of developing wind waves. In (9), it is taken into account that waves starting in the vicinity of the TC eye, inside the circle $\rho < 0.25$, cannot escape this region, due to inflow angle of wind velocity; once generated, these waves spiral towards the calm area of vanishing winds and their development stops. The last multiplier in the first relationship of (9) takes into account that wind waves passing the area of maximal wind speed are not fully developed. Hence, leaving this area, waves start to lose energy due to wave breaking, adjusting the energy balance to reduced wind forcing. Comparing (9) with numerical simulations, Fig.14, it was found that these relationships are valid for radial distances $\rho < \rho_0(\tilde{R}_m)$ with $\rho_0(\tilde{R}_m)$ parameterized as

$$
\rho_0(\tilde{R}_m) = 5\tilde{R}_m^{-0.2}
\tag{10}
$$

At $r/R_m \geq \rho_0(\tilde{R}_m)$ waves evolve as swell systems, for which the wind forcing is switched off. Swell equations can be rewritten as

$$
\begin{aligned}
\partial e^{-2}/\partial r &\propto \lambda_p^{-5} \\
\partial \lambda_p^5/\partial r &\propto e^2
\end{aligned}
\tag{11}
$$

where non-linear dissipation is solely considered. The impact of focusing/defocusing is not taken into account. These effects are negligible during the initial stage of swell evolution. Substituting (8) in (11), with $\tilde{e} = \tilde{H}_s^2/16$), and taking into account the "magic" relationship between the fetch

law constants: $2p + 10q + 1 = 0$ [Badulin et al., 2007], one may find that equations have the same form for f_h^2 (instead of e) and f_λ (instead of λ), and do not dependent on R_m.

For the sake of simplicity, we solve system (11) iteratively, first ignoring the impact of the peak frequency downshift on the energy attenuation. After this first iteration, solutions of equations (11) with boundary conditions, $f_y^s = f_{y0}^w \equiv f_y^w(\rho_0)$ at $\rho = \rho_0$, read:

$$f_h^s(\rho) = f_{h0}^w \left[1 + C_H \left(f_{h0}^w \right)^4 \left(f_{\lambda 0}^w \right)^{-5} (\rho - \rho_0) \right]^{1/4}$$
$$f_\lambda^s(\rho) = f_{\lambda 0}^w \left[1 + \left(c_\lambda / C_L \right) \log \left(1 + C_L \left(f_{h0}^w \right)^4 \left(f_{\lambda 0}^w \right)^{-5} (\rho - \rho_0) \right) \right]^{1/5}$$

(12)

where superscript "s" now notes the regime of swell.

Since φ_p is constant along a swell-train trajectory, the difference between swell and wind directions is solely governed by changes of the wind direction, φ_w, along the swell trajectories. Corresponding relationship for $\varphi_p - \varphi_w$ at $r/R_m \geq \rho_0$ thus reads:

$$f_\varphi^s(\rho) = -\arccos \left[\left(\rho_0/\rho \right) \cos(f_{\varphi 0}^w + \varphi_{in}) \right] - \varphi_{in}$$

(13)

where φ_{in} is the inflow angle of the wind velocity, and $f_{\varphi 0}^w = f_\varphi^w(\rho_0)$. Referring to (13), for $\rho_0/\rho = 1$, swell and wind waves align, while, at large radial distances, $\rho_0/\rho \ll 1$, the swell direction approaches the radial direction.

Combination of wind waves and swell functions, f_y^w and f_y^s correspondingly, then gives the following dimensionless universal functions in (8):

$$f_y = \left[f_y^w - (f_y^w - f_y^s) h(\rho - \rho_0) \right]$$

(14)

where subscript "y" stands for (h, λ, φ), i.e. for SWH, peak wavelength and its direction relative to the wind one, and $h(\rho - \rho_0)$ is a unit step-like function, here specified as $h(\rho - \rho_0) = \left[1 + \tanh \left(3(\rho - \rho_0) \right) \right]/2$.

Parametrizations (8) with universal functions (14) are shown in Fig.14. Self-similar solutions are well consistent with numerical simulations, correctly reproducing wave parameters in the range $r/R_m < 4$ for a wide range of TCs parameters. Note, at large distances (ρ around 6 and 4.5), numerical simulations can take large values of SWH, related to local energy increases in the vicinity of the caustic zones, not taken into account in the suggested self-similar solutions.

To check the proposed solutions for "ordinary" cyclones, moderate winds and R_m of order hundreds km, model simulations are performed with $u_m = 10$m/s and $R_m = 100$ km. Corresponding radial profiles are shown in Fig.14 together with the self-similar solutions. An overall agreement is obtained between, self-similar solutions, originally developed for intense TC conditions, with model simulations. It demonstrates the robustness of these suggested simplified solutions (8) with (14).

6.3. Moving TCs: Maxima of SWH and Wavelength

For the distribution of wave characteristics in the central part of the TC, i.e. $r/R_m < 4$, self-similar solutions are further used to evaluate the impact of the TC movement. First, the maximal values of energy, $e^{\max}$, and wavelength, $L_p^{\max}$, are compared with the self-similar laws (7). For the 63 sets of triplets, $e^{\max}$, $\lambda_p^{\max}$, and deviation of wave direction from the wind velocity, $\varphi_p^{\max} - \varphi_w$, the energy and wavelength are first scaled by the reference values

$$
\begin{aligned}
e_0^{\max} &= a_e \left(u_m^4 / g^2 \right) \tilde{R}_m^p \\
\lambda_{p0}^{\max} &= a_\lambda \left(u_m^2 / g \right) \tilde{R}_m^{-2q}
\end{aligned}
, \tag{15}
$$

where $a_e = 1.4 \times 10^{-6}$ and $a_\lambda = 6.0 \times 10^{-2}$. These constants correspond to maximal energy and associated peak wavelength for a stationary TC, Fig.14. Scaled energy $e^{\max} / e_0^{\max}$ and peak wavelength $\lambda_p^{\max} / \lambda_{p0}^{\max}$ are shown Fig.15 as function of $\tilde{R}_m / \tilde{L}_{cr}^m$ where

$$
\tilde{L}_{cr}^m = c_{cr} \left(u_m / 2V \right)^{1/q}, \tag{16}
$$

and c_{cr} is a constant linked to the fetch-law constants as: $c_{cr} = -c_\alpha^{-1/q} q/(1+q)$. After scaling, these maximal values collapse for different TC conditions, to conform the self-similarity character of wave developments under TCs. Universal functions clearly distinguish slow TCs, $\tilde{R}_m / \tilde{L}_{cr}^m > 1$, from fast TCs, $\tilde{R}_m / \tilde{L}_{cr}^m < 1$. The condition $\tilde{R}_m / \tilde{L}_{cr}^m \approx 1$ corresponds to the group velocity resonance for the largest possible waves generated under a moving TC.

In azimuth, the location of $e^{\max}$ for "slow" TCs is about 50 deg, i.e. at the boundary between the front and the right sectors. For fast TCs, this azimuth location is shifted to the boundary between the TC right and back sectors. Radial location of $e^{\max}$ varies in the range $1 < r/R_m < 1.5$ for slow TCs, and in the range $1.5 < r/R_m < 2$ for fast ones. Deviation of wave direction from the wind

varies from about 40 deg to the right, to about 40 deg to the left, for slow and fast TCs, correspondingly.

For practical applications, the self-similar solutions, shown in Fig.15, can be fitted as

$$
\begin{aligned}
\tilde{e}^{\max} / \tilde{e}_0^{\max} &= l_e + m_e \left(\tilde{R}_m / \tilde{L}_{cr}^m \right)^{n_e} \\
\tilde{\lambda}_p^{\max} / \tilde{\lambda}_{p0}^{\max} &= l_\lambda + m_\lambda \left(\tilde{R}_m / \tilde{L}_{cr}^m \right)^{n_\lambda}
\end{aligned}
\tag{17}
$$

where $\left[l_e, m_e, n_e \right]$ and $\left[l_\lambda, m_\lambda, n_\lambda \right]$ are the fitting constants equal to: [1, 3.84, -0.4] for energy and [1, 1.37, -0.38] for wavelength if $\tilde{R}_m / \tilde{L}_{cr}^m \geq 1$ (slow TC); and equal to [0, 2.92, 0.53] for energy and [0, 1.67, 0.31] for wavelength if $\tilde{R}_m / \tilde{L}_{cr}^m < 1$ (fast TC).

Equations (17) can be rewritten in the form of standard fetch laws:

$$
\begin{aligned}
\tilde{e}^{\max} &= c_e \tilde{X}_e^{\,p} \\
\tilde{\lambda}_p^{\max} &= c_\lambda \tilde{X}_\lambda^{\,-2q}
\end{aligned}
$$

using the "equivalent fetch" $\tilde{X}_e$ and $\tilde{X}_\lambda$, and c_e and c_λ following 1D fetch-law constants, specified in present study as $c_e = 1.3 \times 10^{-6}$ with $p = 3/4$, and $c_\lambda = 2\pi c_\alpha^{-2} = 4.51 \times 10^{-2}$ at $c_\alpha = 11.8$ with $q = -1/4$ [see Appendix B in Part 1]. The equivalent fetch defined from (15) and (17) for the energy and wavelength, read

$$
\begin{aligned}
\tilde{X}_e &= 1.1 \times \tilde{R}_m \left[l_e + m_e \left(\tilde{R}_m / \tilde{L}_{cr}^m \right)^{n_e} \right]^{1/p} \\
\tilde{X}_\lambda &= 1.8 \times \tilde{R}_m \left[l_\lambda + m_\lambda \left(\tilde{R}_m / \tilde{L}_{cr}^m \right)^{n_\lambda} \right]^{-1/(2q)}
\end{aligned}
\tag{18}
$$

where the constants come from $\left(a_e / c_e \right)^{1/p} = 1.1$ and $\left(a_\lambda / c_\lambda \right)^{-1/(2q)} = 1.8$. These equivalent fetch expressions can then be substituted into the fetch-laws to provide fast estimates of maximal values of energy and wavelength of waves generated by a moving TC.

Comparisons of the equivalent fetch expressions (18) with the empirical relations suggested by Young [1988] and Young and Vinoth [2013], evaluated for the considered set of 63 TCs, are shown in Fig.16. The empirical relationships are not self-similar with TC parameters, u_m, R_m,

and V, leading to rather large spreading, Fig.16, left. Nevertheless, the model solutions are quantitatively consistent with empirical values: comparable maximal values are found for an equivalent fetch around the resonance, $R_m/L_{cr}^m = 1$, and a decrease of the fetch towards smaller and larger values of R_m/L_{cr}^m. The model equivalent fetch, plotted as function of maximal wind speed and translation velocity, Fig.16-right, provides values in agreement with Young and Vinoth [2013].

6.4. *Moving TC: Self-Similarity in 2D Distributions*

Besides these maximal values, it is also tempting to check whether 2D spatial distributions of SWH and the peak wavelength and its direction obey the self-similar distributions in form (7). For that purpose, each of the TCs' fields are divided by boxes, shown in Fig.1. Each of the boxes containing a number of different rays (see example in Fig.10), the ray corresponding to the longest wavelength is selected as the primary generated wave system. Then, the energy and wavelength of this primary wave train are: (i) scaled by local wind speed and gravity acceleration; (ii) normalized by its corresponding stationary values; and (iii) represented in form (7), as function of TC azimuth and radius normalized by critical fetch (6) defined for the local wind speed.

These fields of primary wave system parameters,- normalized energy and wavelength, wave direction relative to the wind, represented in self-similar form (7), are further averaged over the ensemble of 63 considered TCs, and showed Fig. 17.

Figure 17 is about here

The lower rows in Fig.17 provide standard deviation of "individual" TC fields from the overall mean. Except in the vicinity of $r/L_{cr} = 1$, where wave parameters exhibit rapid changes when the group velocity resonance ends, values of the normalized standard deviation are rather small. Fields of waves generated by a TC, being represented in the universal variables (7), thus largely merge. Hence self-similarity in the suggested form (7) certainly applies. The universal functions freely available at link https://zenodo.org/record/4122473#.X5MxS-1n2Uk.

Functions presented in Fig.17 correspond to 2D dimensionless universal functions Φ_λ, Φ_e and Φ_φ in (7). Transects of these functions over the TC azimuth at fixed r/L_{cr} provides azimuthal distributions of the primary wave system direction relative to that in stationary TC, and the energy and wavelength system scaled by corresponding values for stationary TC. As it follows from Fig.17, the storm area of the same TC can be divided on an inner area, $r/L_{cr} < 1$, where

generated waves "feel" TC as a fast, and the outer area, $r/L_{cr} \geq 1$, where generated waves are subjected to the local group velocity resonance and thus attain an "abnormal" development.

Self-similar solutions are mostly valid within the TC high wind area where a majority of the primary wave system originates, to then turn into the regime of swell. Referring to Fig.7, Fig.8 and Fig.10, this area should be limited to $r/R_m < 3$. Outside this area, primary wave systems travel as swell systems. A swell system can approximately be treated as free propagating waves, with dynamics apparently not depending upon scaling parameters used in (7).

<mark>Figure 18 is about here</mark>

6.5. Case studies

Fig.18 presents comparisons between azimuthal distributions of the self-similar solutions for SWH, period and direction of the primary wave systems with airborne measurements reported by Hwang and Fan [2017, their Fig 13, cases B24 and I14] and by Hwang et al. [2017, their Fig.8] for TC Bonnie 1998 and Ivan 2004. Model simulations were performed using the radial wind speed profile (1), with inflow angle 20 deg, and the following TCs parameters: $u_m = 44$ m/s, R_m =74 km, and $V = 4.5$ m/s for TC Bony; $u_m = 50$ m/s, $R_m = 50$ km, and $V = 5$ m/s for TC Ivan.

Model simulations shown in Fig.18 represent azimuthal behavior of the self-similar solutions (7) for specified TC parameters at fixed radius. Azimuthal behavior for each of the wave parameters, originates from transect of corresponding dimensionless universal functions, Φ_λ, Φ_e and Φ_φ shown in Fig.17, over TC azimuth at fixed value of r/L_{cr}. As obtained, the model reproduces very well the magnitudes and the azimuthal modulations of observed SWH and wave period, Fig.18, left- and mid-plot.

For wave direction, model outputs and measurements are compared on quantitative level at radial distances $r/R_m > 1$. At smaller radial distances the data demonstrate a peculiar behavior that differs from "regular" azimuthal undulations of wave directions relative to the wind one at $r/R_m > 1$.

According to the model, such behavior results from the decrease of wind speed towards the eye at small radial distances. As a consequence, parameter r/L_{cr} also decreases towards the eye, and within the inner core area it falls below 1, $r/L_{cr} < 1$. Waves generated inside this inner area can be treated as waves under fast TC. Thus, as discussed above, once generated in the front sector, these waves travel backwards through the complex wind velocity around the eye, and appear in

the back sector sector as swell opposing to the wind. Open triangles in Fig.18-right show model simulations of the wave peak direction at radial distances r/R_m from 0.1 to 0.3. Models simulations reproduce peculiar behaviour of the measurements which were obtained at the smallest radial distances. Notice that that we cannot plot in Fig.18-right the self-similar solution for small radial distances, since its validity is limited by $r/R_m > 0.25$ due to discussed above limitations in the stationary solutions (9).

7. Discussion

A clear advantage of the self-similarity approach is to rapidly assess wave space-time distributions under different TCs, characterized by u_m, R_m, and V.

As an example, Fig.19 displays fields of SWH, peak wavelength and directions, generated by TCs with different parameters derived from solution (7) with the universal function shown in Fig.17. Validity of these fields is restricted to the area $r/R_m < 3$. Comparing Fig.19 with Fig.7, where overlapping of wave-trains rays is shown, reconstructed fields may appear 'blurred" compared with ray composition, but stay quantitatively very close.

The self-similar solutions (7) can thus be treated as TC-wave Geophysical Model Function (TC-wave GMF), to help rapidly derive 2D field of primary wave system parameters (SWH, wavelength, direction) to assess impacts of different input parameters u_m, R_m, and V.

The primary wave systems predicted by the TC-wave GMF on the outer radius, $r/R_m = 3$, can be further used as the boundary conditions for swell propagation, Eqs.(47) to (50) in Part 1. In these equation the wind forcing is switched off, but the angular dispersion term, first term in r.h.s. of eq. (47), plays the important role in swell energy evolution. This term can be estimated from the azimuthal distribution of wave directions along the contour $r/R_m = 3$.

The suggested self-similar description is the result of a fitting procedure applied to numerical solutions of 2D parametric models obtained for a very idealized wind field, with radial profile (1) and inflow angle 20 deg. Applicability of the universal functions Φ_λ, Φ_e and Φ_φ in self-similar solution (7) for other type of wind velocity fields may be questionable, and shall require additional investigations.

Yet, wave development must be understood to be spread in space and time. Waves at a given location are not directly linked to the local wind, but depend on the wind velocity field integrated along the trajectory of the developing wave train. A typical spatial scale of wave development is

of the order of the TC radius. Hence, scales for the wind field, relevant to the wave development, should be about r in radial direction and about $\pi/2$ in azimuthal direction. Since, the exact shape of the wind profile is not important, we may thus anticipate that the universal function Φ_λ, Φ_e and Φ_φ in (7) can also be used for more realistic (and averaged) wind field, which can even be azimuthally anisotropic. Considering information on radial distribution of wind speed, $r34$, $r50$, and $r64$, for different quadrants, along with R_m and u_m, 2D functions in polar coordinates system can be used to calculate the reference (for stationary TC) distribution (8) with (14) and corresponding values of the universal functions Φ_λ, Φ_e and Φ_φ. Self-similar solutions (7) will then provide spatial distribution of SWH, peak wavelength and direction of waves under TC with arbitrary wind field.

8. Conclusion

In this paper, the revised 2D-parametric model [Kudryavtsev et al., companion paper] has been applied to predict wave field developments under moving TCs, and to assess their consistencies with available observations.

The model set of equations describing either wind waves development and swell evolution, was solved using the method of characteristics. Wave-rays patterns provide straightforward visualization on how the wave trains originating from different areas under the TC, develop and travel through the varying wind velocity field, until leaving the storm area as swell systems.

Compared with stationary TC conditions, TC motions introduce remarkable azimuthal anisotropy in the wave-ray patterns and wave-trains dynamics. Wave trains starting in the lower-half of the R-S and the right-half of B-S can be subject to the group velocity resonance. It means that the group velocity of a developing wave-train matches the TC translation velocity at some point, the turning point. At this point, the wave train direction, relative to the TC motion, changes from backwards to forward. This effect increases the residence time of the wave-train in TC strong forcing area, leading to large wave growth. The larger the TC translation velocity, the longer will be the waves subject to group velocity resonance. The energy of TC-generated waves will then also be larger the faster the TC moves. But if the TC translation velocity exceeds a threshold value, TC-generated waves cannot reach group velocity resonance, and in their course of development, will travel backwards, forming a wake of swell systems left behind the forwardly moving TC.

The superposition of a large number of wave-trains rays starting from different location, exhibit coherent patterns for the spatial distribution of wave parameters, SWH, peak wavelength and

direction depending on TC characteristics, - maximal wind speed, radius, and translation velocity, Fig.7 and Fig.8. The group velocity resonance results in maximal wave energy at the boundary between R-S and F-S. Wave trains further travel as swell systems through TC F-S sector, in direction of the TC heading.

Model simulations are consistent with the observations reported e.g. in [Hwang and Walsh, 2018; Hwang and Fan, 2017; Hwang et al. 2017; Young and Vinoth, Young 2017], and produce wave field features under TCs which are similar to that had already been known from numerical simulations using sophisticated wave models, e.g. WWIII model [Moon et al., 2003; Liu et al., 2017]. Accordingly, the suggested 2D parametric model can be considered as an effective tool to provide large ensembles of solutions, to test different TC characteristics to help forecast TC dynamics.

The energy and the momentum source terms to prescribe the 2D parametric model were designed to reproduce fundamental 1D self-similar laws of wave development. This questioned whether wave fields under TCs could also obey 2D self-similar distributions. Analysis of a set of model outputs for 63 TCs, spanning the range of different parameters, confirms that 2D self-similar solutions exist either for stationary TC, Eqs (8) with (14), and for moving TC, relationship in form (7).

Suggested self-similar solutions, Eq. (10), then provide immediate estimates of maximal wave parameters, - SWH, wavelength, and direction, generated by TC with arbitrary u_m, R_m, and V. Shape of the derived universal functions clearly divides TCs between two family-types: slow TCs which parameters satisfy the conditions $\tilde{R}_m / \tilde{L}_{cr}^m > 1$, and fast TCs such that $\tilde{R}_m / \tilde{L}_{cr}^m < 1$, where $\tilde{L}_{cr}^m$ is defined by (16). The region $\tilde{R}_m / \tilde{L}_{cr}^m \approx 1$ corresponds to the group velocity resonance with the largest possible waves generated by a TC.

A clear advantage of the self-similarity solutions is that any and numerous scenarios of wave generation by TCs can immediately be assessed on quantitative level. In a certain sense, 2D self-similar solutions (7) can be treated as TC-wave Geophysical Model Function (TC-wave GMF), to help analytically derive 2D field of the primary wave system parameters (SWH, wavelength, direction) under TC prescribed by u_m, R_m, and V. The 2D self-similar solution (7) with universal functions freely available at link https://zenodo.org/record/4122473#.X5MxS-1n2Uk.

Comparisons between the proposed self-similar solutions with measurements of TC-generated waves reported in the literature [Young and Vinoth, 2013; Young, 2017; Hwang and Walsh, 2018; Hwang and Fan, 2017; Hwang et al., 2017], see Sec. 5.2, 6.3 and 6.5, demonstrate very

good agreement. This is encouraging and may warrant use of either 2D parametric model and/or self-similar solutions based on parametrization of 2D parametric model simulations, for practical and research applications.

References

Badulin S. I., A. V. Babanin, V. E. Zakharov, and D. Resio (2007), Weakly turbulent laws of wind-wave growth, *J. Fluid Mech., 591,* 339–378, doi:10.1017/S0022112007008282.

Bowyer, P. J., and A. W. MacAfee (2005), The theory of trapped-fetch waves with tropical cyclones - An operational perspective, *Weather Forecasting, 20,* 229–244, doi:10.1175/WAF849.1.

Combot, C., A. Mouche, J. Knaff, Y. Zhao, Y. Zhao, L. Vinour, Y. Quilfen, and B. Chapron (2020), Extensive high-resolution Synthetic Aperture Radar (SAR) data analysis of Tropical Cyclones: comparisons with SFMR flights and Best-Track. *Mon. Wea. Rev*., doi: 10.1175/MWR-D-20-0005.1.

Dulov V., V. Kudryavtsev, and E. Skiba (2020), On fetch and duration-limited wind wave growth: data and parametric model. *Ocean Modelling, 153*, 101676, doi: 10.1016/j.ocemod.2020.101676

Dysthe, K. B., and A. Harbitz (1987), Big waves from polar lows?, *Tellus, Ser. A, 39*, 500–508, doi:10.1111/j.1600-0870.1987.tb00324.x.

Holland, G. J. (1980), An analytical model of the wind and pressure profiles in hurricanes, *Mon. Weather Rev., 108*, 1212–1218, doi:10.1175/1520-0493(1980)108<1212:AAMOTW>2.0.CO;2.

Hwang P., and E. Walsh (2018), Propagation Directions of Ocean Surface Waves inside Tropical Cyclones*, J. Phys. Oceanogr., 48 (7),* 1495-1511, DOI:10.1175/JPO-D-18-0015.1

Hwang P, and Y. Fan (2017), Effective fetch and duration of tropical cyclone wind fields estimated from simultaneous wind and wave measurements: Surface wave and air–sea exchange computation, *J. Phys. Oceanogr., 47*, 447–470, DOI:10.1175/JPO-D-16-0180.1.

Hwang P., Y. Fan, F. J. Ocampo-Torres, and H.García-Nava (2017), Ocean surface wave spectra inside tropical cyclones. *J. Phys. Oceanogr., 47*, 2393–2417, doi: 10.1175/JPO-D-17-0066.1.

Jullien, S., J. Aucan, J. Lefèvre, A. Peltier, and C.E. Menses (2020), Tropical cyclone induced wave setup around New Caledonia during cyclone COOK (2017), *Journal of Coastal Research*, Special Issue No. 95, 1454-1459 (2020). https://doi.org/10.2112/SI95-281.1

Quilfen, Y., B. Chapron, and J. Tournadre (2010), Satellite microwave surface observations in tropical cyclones. *Monthly Weather Review,* 138(2), 421–437. https://doi.org/10.1175/2009MWR3040.1

Quilfen, Y., J. Tournadre, and B. Chapron (2006), Altimeter dual-frequency observations of surface winds, waves, and rain rate in Tropical Cyclone Isabel. *J. Geoph. Res.,* 111, C01004. https://doi.org/10.1029/2005JC003068

King, D. B., and O. H. Shemdin (1978), Radar observations of hurricane wave directions, in *Proceedings of 16th International Conference on Coastal Engineering*, pp. 209–226, Am. Soc. of Civ. Eng., Hamburg, Germany

Kitaigorodskii, S.A. (1962), Applications of the theory of similarity to the analysis of wind-generated water waves as a stochastic process, *Bull. Acad. Sci. USSR Geophys. Ser., 1*, 105–117.

Kudryavtsev, V., P. Golubkin, and B. Chapron (2015), A simplified wave enhancement criterion for moving extreme events, *J. Geophys. Res. Oceans, 120,* 7538-7558, doi:10.1002/2015JC011284

Kudryavtsev V. M. Yurovskaya, and B. Chapron (companion paper), 2D parametric model for surface wave development in wind field varying in space and time, *J. Geoph. Res*., this issue.

Liu Q., A. Babanin, Y. Fan, S. Zieger, C. Guan, and I.-J. Moon (2017), Numerical simulations of ocean surface waves under hurricane conditions: Assessment of existing model performance, *Ocean Modelling.* 118, 73-93, doi: 10.1016/j.ocemod.2017.08.005.

Moon, I.-J., I. Ginis, T. Hara, H. L. Tolman, C. W. Wright, and E. J. Walsh (2003), Numerical simulation of sea surface directional wave spectra under hurricane wind forcing, *J. Phys. Oceanogr., 33,* 1680–1706, doi:10.1175/2410.1.

Mouche, A., B. Chapron, J. Knaff, Y. Zhao, B. Zhang, and C. Combot (2019), Co-polarized and cross-polarized SAR measurements for high-resolution description of major hurricane wind structures: Application to Irma category 5 hurricane. *J. Geoph. Res. Oceans*, 124, 3905– 3922. https://doi.org/10.1029/2019JC015056

Walsh E. J., and Coauthors (2002), Hurricane directional wave spectrum spatial variation at landfall. *J. Phys. Oceanogr.,* 32, 1667–1684, https://doi.org/10.1175/1520-0485(2002)032,1667:HDWSSV.2.0.CO;2.

Wright, C. W., and Coauthors (2001), Hurricane directional wave spectrum spatial variation in the open ocean. *J. Phys. Oceanogr.*, 31, 2472–2488, https://doi.org/10.1175/1520-0485(2001) 031,2472:HDWSSV.2.0.CO;2.

Young, I. R. (1988), A parametric hurricane wave prediction model, *J. Waterw. Port Coastal Ocean Eng., 114(5)*, 637–652, doi:10.1061/(ASCE)0733-950X(1988)114:5(637).

Young, I. R. (2006), Directional spectra of hurricane wind-waves, *J. Geoph. Res.*, 111, C08020, https://doi.org/10.1029/2006JC003540.

Young, I. R., and J. Vinoth (2013), An ''extended fetch'' model for the spatial distribution of tropical cyclone wind-waves as observed by altimeter, *Ocean Eng., 70,* 14–24, doi:10.1016/j.oceaneng.2013.05.015.

Young, I.R. (2017), A Review of Parametric Descriptions of Tropical Cyclone Wind-Wave Generation. *Atmosphere,* 8, 194.

Zhang, J. A., and E. W. Uhlhorn (2012), Hurricane Sea Surface Inflow Angle and an Observation-Based Parametric Model. *Mon. Wea. Rev*., 140, 3587–3605, https://doi.org/10.1175/MWR-D-11-00339.1.

Zhang, L., and L. Oey (2019), An observational analysis of ocean surface waves in tropical cyclones in the western North Pacific Ocean. *J. Geoph. Res. Oceans*, 124, 184–195. https://doi.org/10.1029/2018JC014517

Figures and Captions
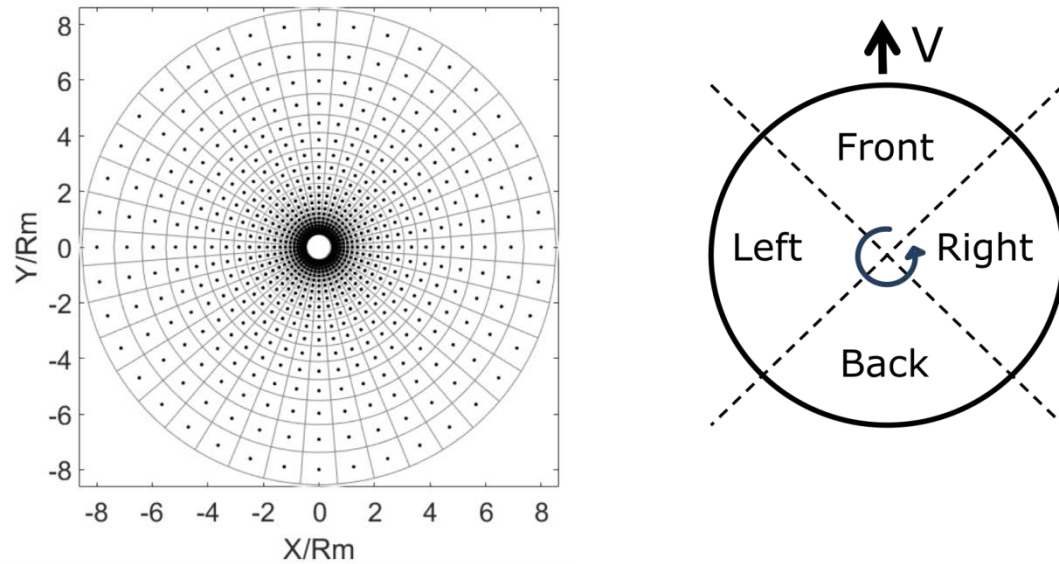
Figure 1. (left) Grid in polar coordinate system where wave-trains were initiated (seeded). Polar "squares" around each of the points, indicate the area where the passing trains are counted and quantified. (Right) Division of TC area on Front-, Left-, Back-, and Right-Sectors (F-S, L-S, B-S, and R-S correspondingly) used throughout the paper.
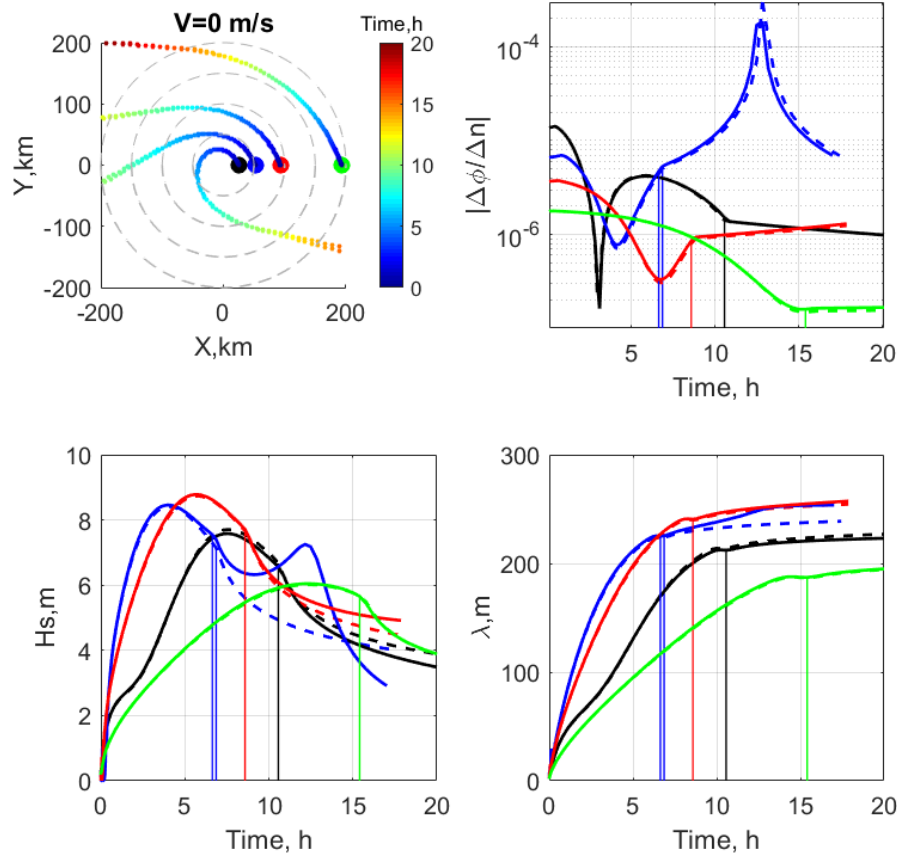
Figure 2. (Upper-left) example of wave-trains trajectories under stationary TC with u_m =50m/s, R_m =50km, and evolution of wave-trains parameters: (lower-left) significant wave height (SWH), (lower-right) peak wavelength, and (upper-right) parameter of the angular focusing (term G_n in (47) from Part 1). Varying color of each of the ray in upper-left plot indicates current time according to the color bar; and the color dots indicate initial positions of selected wave-rays. The same color (as the dots color) is used in other plots to mark time evolution of wave parameters along a given ray. Solid lines of the same style indicate evolution of wave parameters for the full model, and dashed lines indicate calculations without accounting for the effect of the wave ray focusing. Vertical lines indicate travel time when wave-train inverse wave age $\alpha \equiv u\cos(\varphi_p - \varphi_w)/c_p = 0.85$, and consequently wave-train turns from wind-forced regime to the swell one.
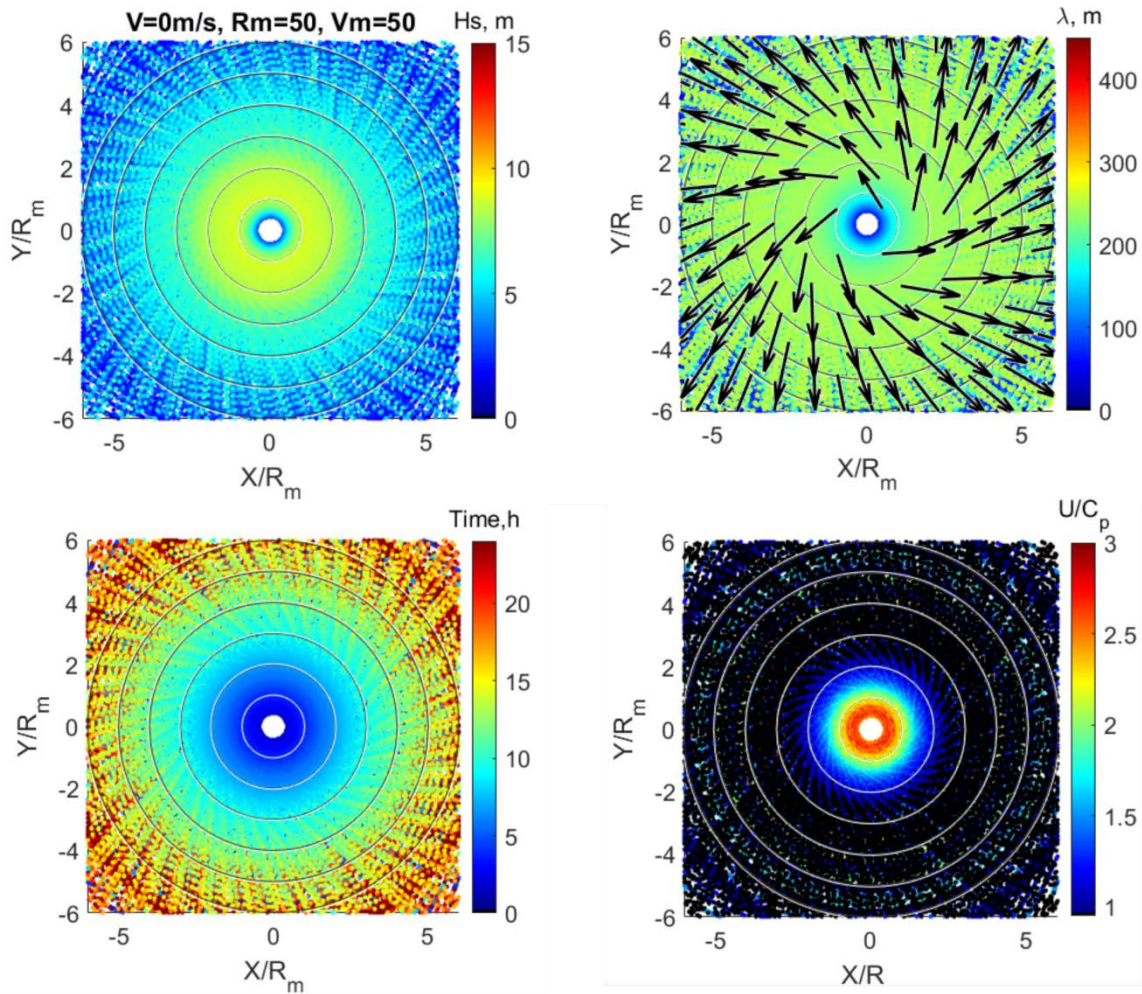
Figure. 3. Composition of rays of wave-trains initially seeded in polar grid shown in Fig 1a One grid-point produces one ray. Wave parameters along the rays are: (upper-left) SWH, (upper-right) spectral peak wavelength, (lower-left) local travel time, and (lower-right) inverse wave age. Each of the plots represents composition of the overlapped rays; ray with the larger local wavelength is on top of other. TC parameters are: R_m=50 km, u_m=50 m/s. Black arrows in the wavelength plot indicate direction of the wavenumber vector.
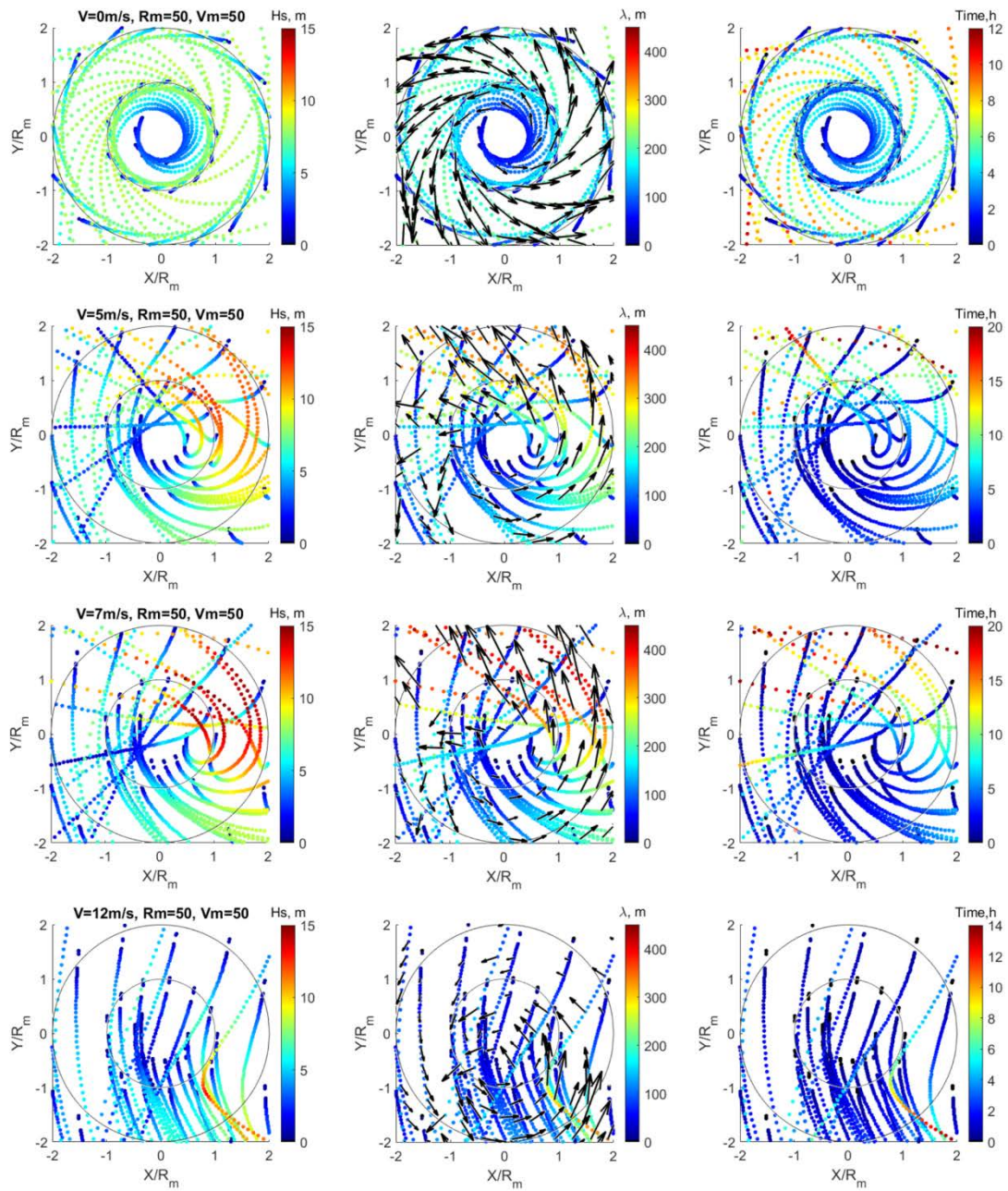
Figure 4. Maps of the wave-trains rays started at radial distances $[R_m/2, R_m, 2R_m, 4R_m]$ with azimuthal step 30 deg. One grid-point produces one ray. Wave parameters along the rays are: (left column) SWH, (mid column) spectral peak wavelength, (right column) local travel time. Black arrows in plots of wavelengths indicate direction of the wavenumber vector and size of the arrow is proportional to wavelength. TC parameters are: R_m =50 km, u_m =50 m/s, translation velocities (rows from top-to-bottom) are 0m/s, 5m/s, 7m/s and 12m/s.
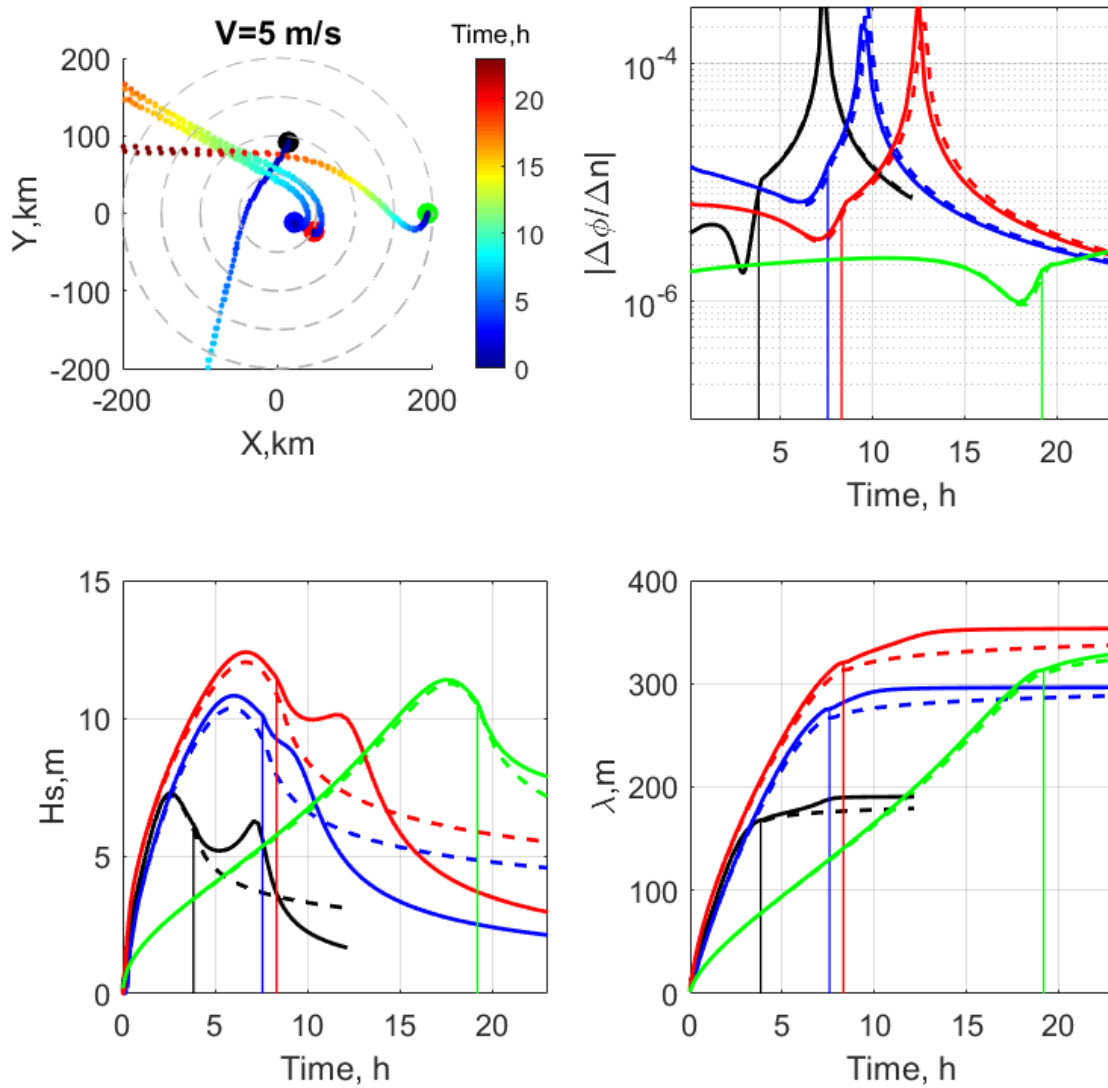
Figure 5. Examples of time-evolution of wave-trains parameters under TC with u_m =50m/s and R_m =50km, and translation speed V =5m/s. Varying color of each of the ray in the upper-left plot indicates travel time according to the color bar; and the color dots indicate initial positions. The same color (as the dots color) is used in other plots to mark time evolution of wave parameters along a given ray. Solid lines of the same style indicate evolution of wave parameters for the full model, and dashed lines indicate calculations without accounting for the effect of the wave ray focusing. Vertical lines indicate local time when wave-train turns from wind force regime to swell one.
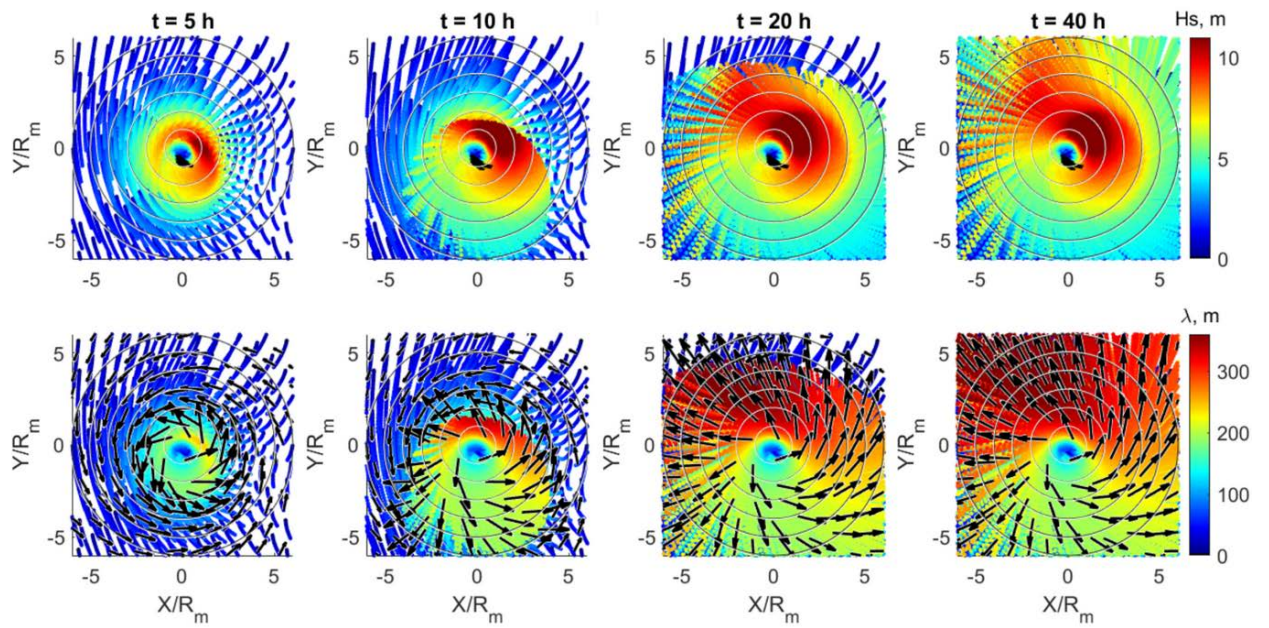
Figure 6. Evolution in time of superposition of wave train rays started on polar grid shown in Fig.1. Parameters of wave trains along the rays are: (upper row) SWH and (lower row) peak wavelength. Black arrows indicate direction of the wavenumber vector. Each of the columns presents superposition of the rays on time moment (columns from left to right): 5, 10, 20 and 40 hours. One grid-point produces one ray. Ray with the largest local wavelength is on top of others. TC parameters are: R_m =50 km, u_m =50 m/s, V =5m/s.
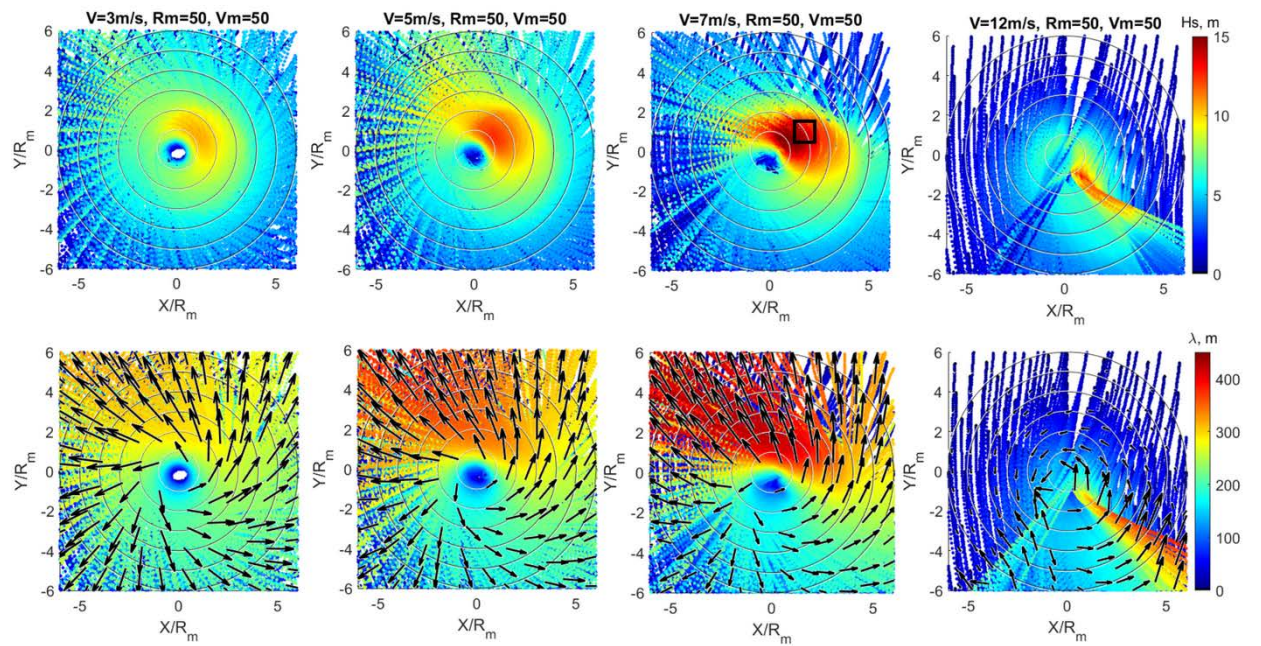
Figure 7. Composition of the wave-trains rays generated by TC with R_m =50 km, u_m =50 m/s, and translation velocities V =3, 5, 8, and 12m/s (columns from left to right correspondingly). Upper row is SWH, H_s, and the lower row is wavelength, λ_p, along the rays. Values of H_s and λ_p are indicated by color with corresponding color-bar. Black arrows indicate wavenumber directions and their length is proportional to the wavelength.
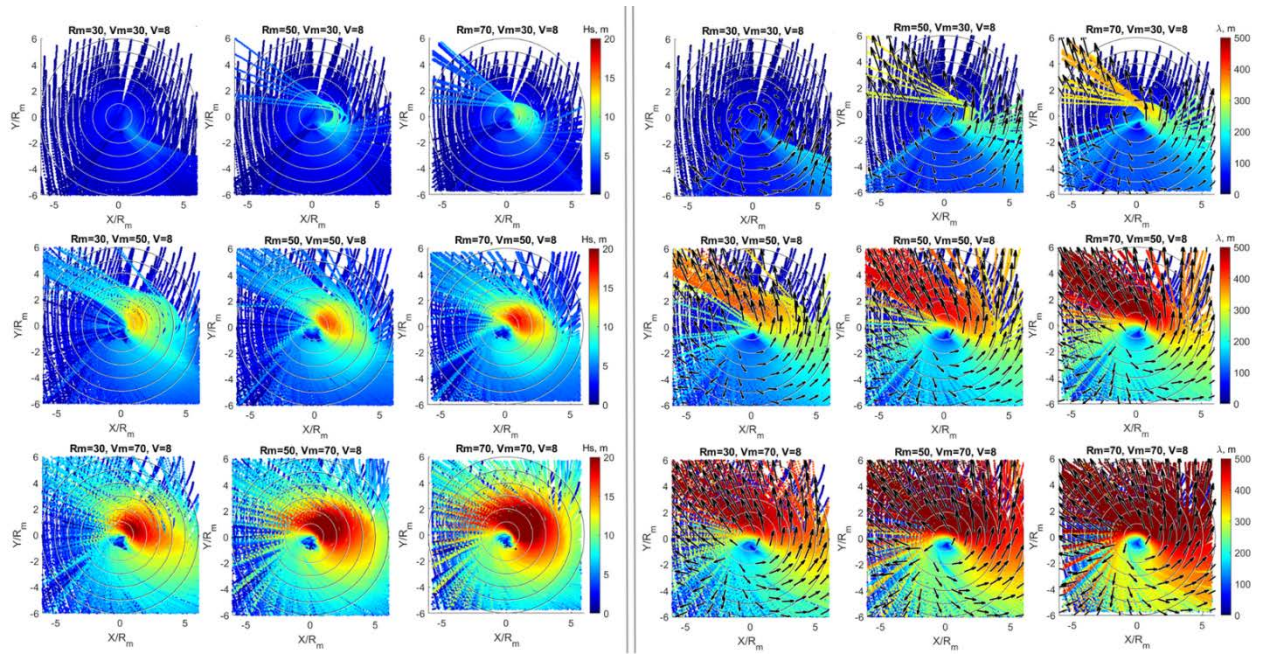
Figure 8. Fields of (left block of plots) SWH and (right block of plots) peak wavelength resulting from composition of the wave-trains rays generated by TC with V =8m/s and with R_m =[30 50 70] km (columns from left to right) and u_m = [30 50 70]m/s (rows from top to bottom). Values of H_s and λ_p are indicated by color with corresponding color-bar. Black arrows indicate wavenumber directions and their length is proportional to the wavelength.
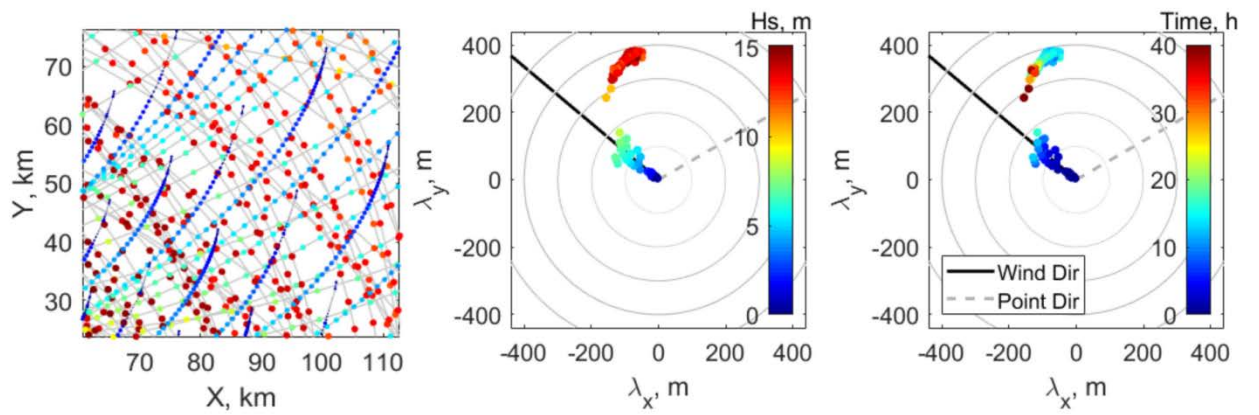
Figure 9. (left) Trajectories of wave trains (dotes connected by the line) passing through the box shown in Fig.7. Color of the dots indicate instant value of SWH shown in color-bar in mid plot. Distribution of (mid) SWH and (right) travel time over wavelengths and directions of trains fallen into the box. Black radial lines in mid and right lots indicate wind direction, and dash line – direction of the box location in TC.
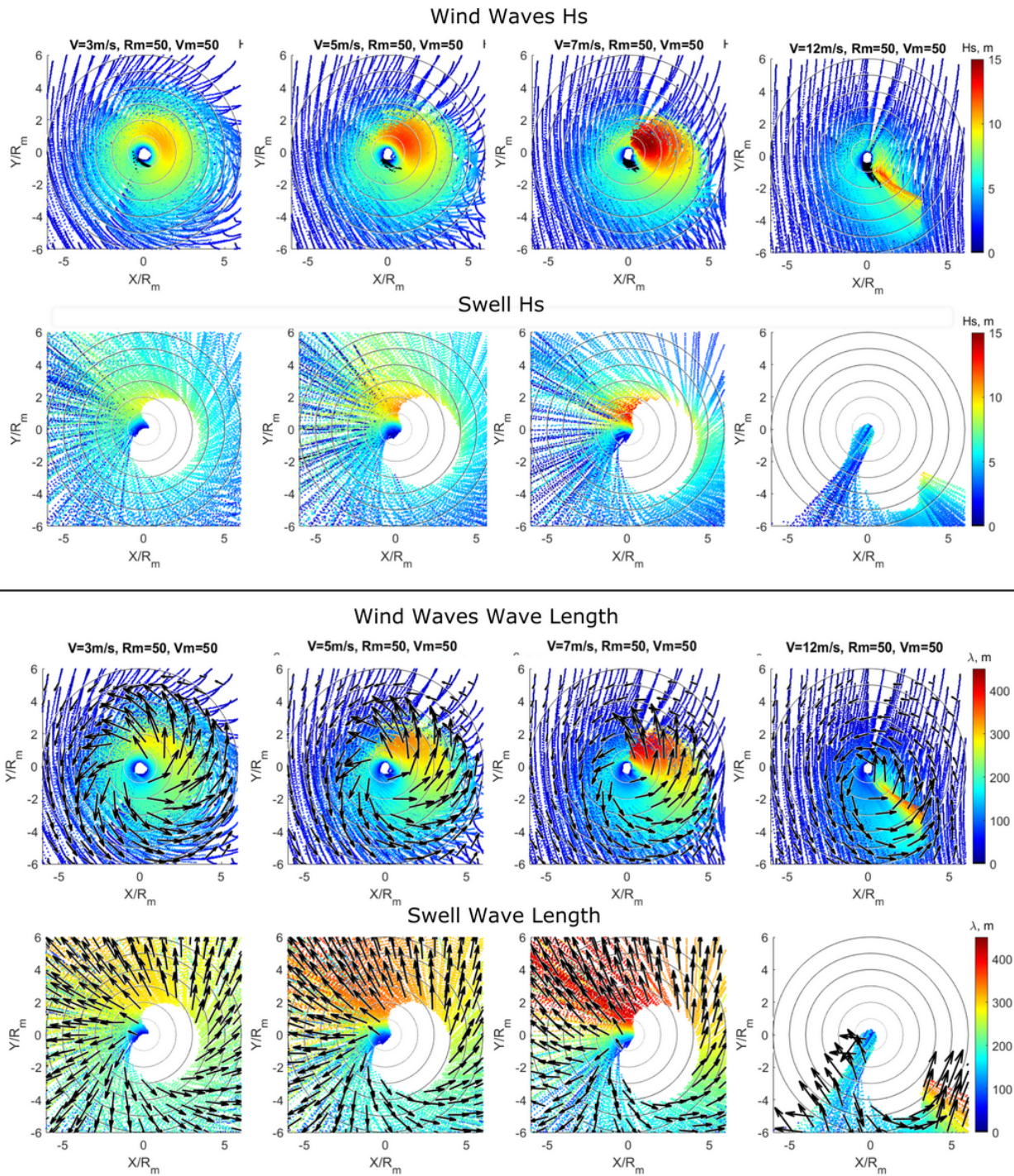
Figure 10. Decomposition of wave fields shown in Fig.7 on wind-waves (first, H_s, and third, λ_p, rows from the top) and swell (second, H_s, and forth, λ_p, rows from the top) systems. Columns from left to right correspond to different TC translation velocities: 3, 5, 7, and 12m/s correspondingly, with R_m=50km and u_m=50m/s. Black arrows indicate direction of waves and their length is proportional to the wavelength.
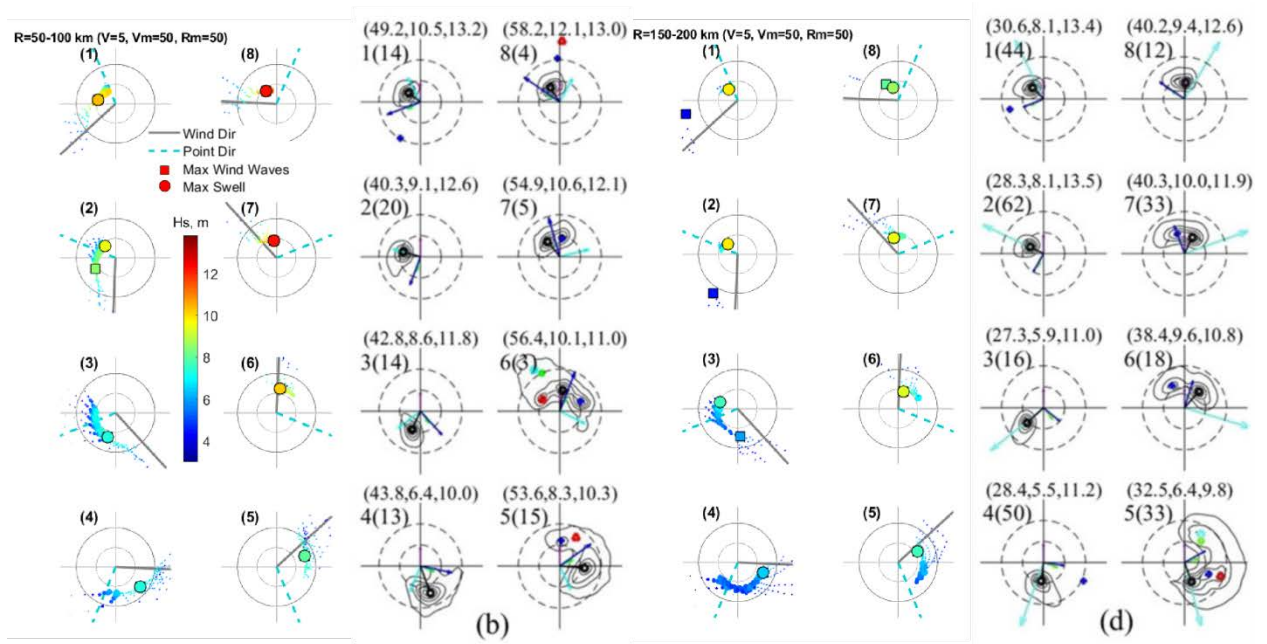
Figure 11. Model (first and third set of plots) and observed (second and third sets) directional spectra in 8 azimuthal slices with width 45 deg distribution from TC heading counter-clockwise (slice number shown in the upper-left corner) in radial distances (left pair of model and observed sets) from 50 to 100 km and (right pair of model and observed sets) from 150 to 200 km. Observed spectra are taken from Hwang and Walsh [2018, their Fig.4e, see also caption to this figure for details]. Circles (solid in model spectra and dash in observed) correspond to wavenumber 0.025 rad/m and 0.05 rad/m. In the model spectra, black lines indicate wind direction, and blue-dashed lines – azimuthal position in TC. Contoured circles and square indicate the dominant swell and wind wave systems, and their color corresponds to the energy indicated in the color-bar. Other (un-contoured) circles of different size are wave trains that ever passed the given azimuth-range sector, their size is proportional to the train energy scaled by maximal value of train energy in given azimuth-range sector.
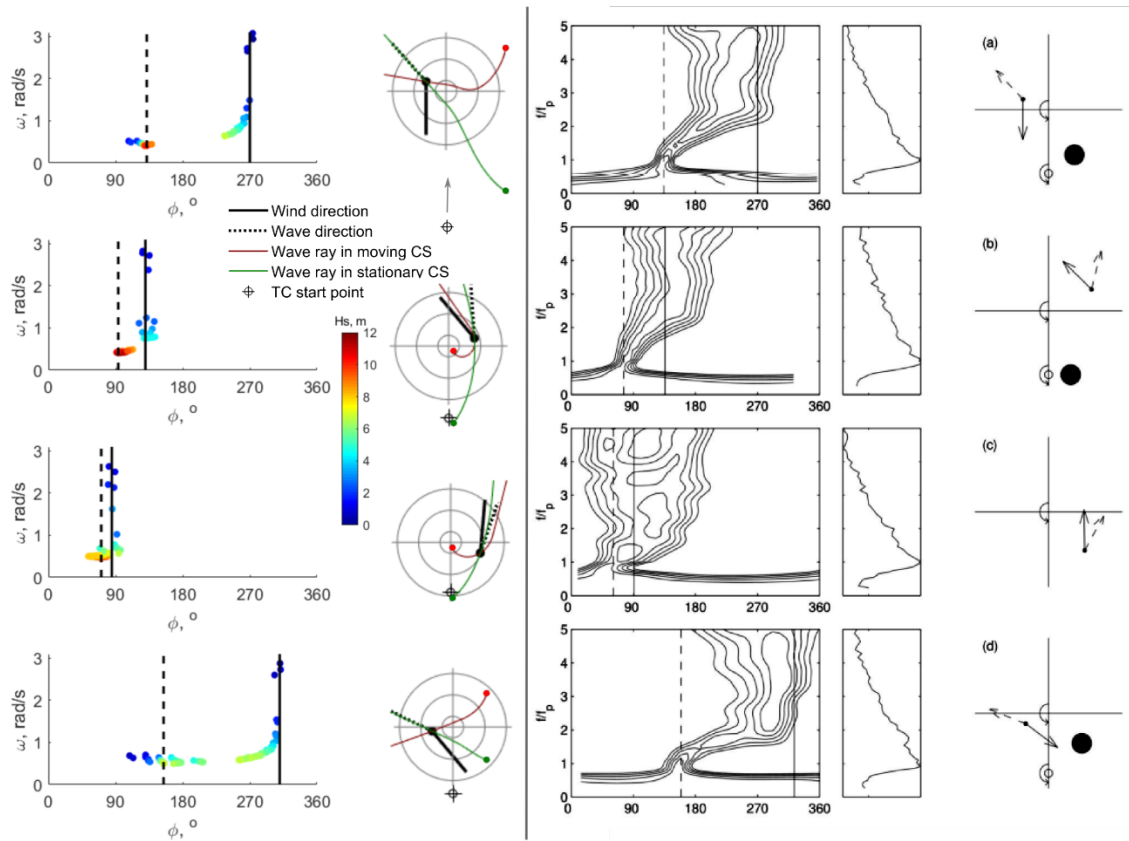
Figure 12. Left half: (Left column) Histograms ("spectra") of wave trains passing the area around the black points (points of "measurements") indicated in the right column. (Right column) Primary wave rays in (green lines) stationary and (red lines) moving coordinate systems. Open circles indicate TC eye locations when wave trains started. Black solid and dotted lines are wind and primary wave directions, correspondingly. TC parameters are R_m=50km and u_m=50m/s, V=7m/s. Gray circles indicate Rm, 3Rm and 5Rm. Right half: Fig. 9 taken from Young [2017] showing directional spreading functions of waves measured at points marked with small solid dots in right column. Large black circles and open circles indicate plausible position where the measured waves started and corresponding position of TC eye.
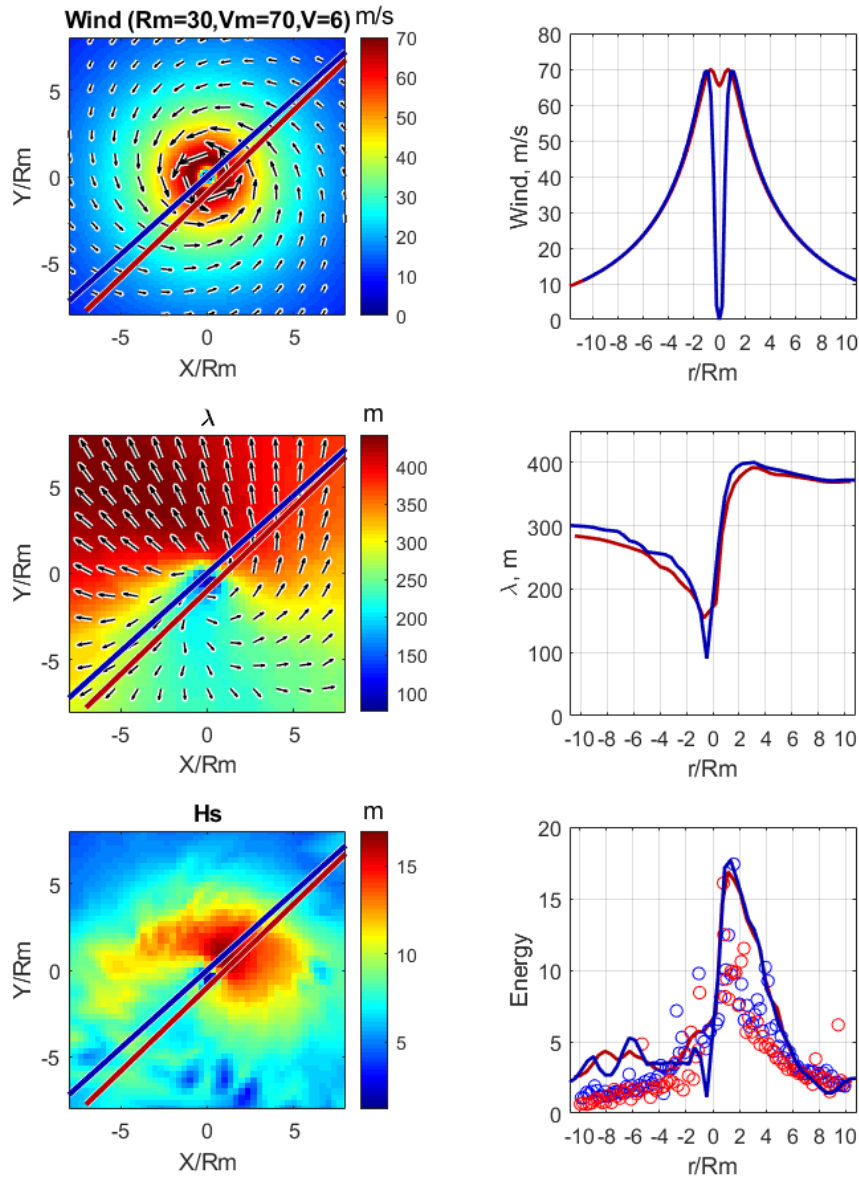
Figure 13. Model simulations and altimeter observations of wind waves under TC Isabel and Songda. (Left column) Model fields of (top) wind, (mid) peak wavelength and direction, and (bottom) SWH; red and blue lines in plots indicate positions of altimeter tracks. (Right column). Transects of the fields shown in the left column along the altimeter tracks. Circles in the bottom plot are altimeter measurements taken from [Kudryavtsev et al., 2015; their Fig.4 and Fig.5]. Blue/Red lines and symbols correspond to TC Isabel/Songda correspondingly.
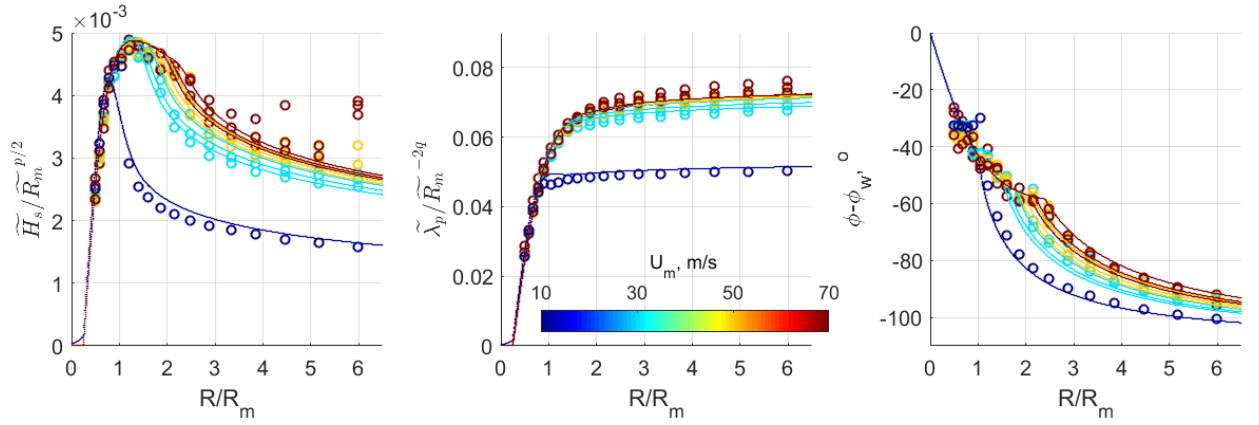
Figure 14. Radial profiles of (left plot) dimensionless SWH normalized by $\tilde{R}_m^{p/2}$: $\tilde{H}_s / \tilde{R}_m^{p/2}$, (mid plot) peak wavelength normalized by $\tilde{R}_m^{-2q}$: $\tilde{\lambda}_p / \tilde{R}_m^{-2q}$, and (right plot) wave peak direction relative to the wind. Open circles show the model simulations for nine stationary TCs with different combination of $u_m = [30, 50, 70]$ m/s and $R_m = [30, 50\ 70]$ km and one "regular" cyclone with Rm=100km and um=10m/s (the lowest line). Lines correspond to self-similar solutions (8) with (14). Color of circles and lines indicate wind speed in accordance with color-bar. Different lines of the same color correspond to different R_m
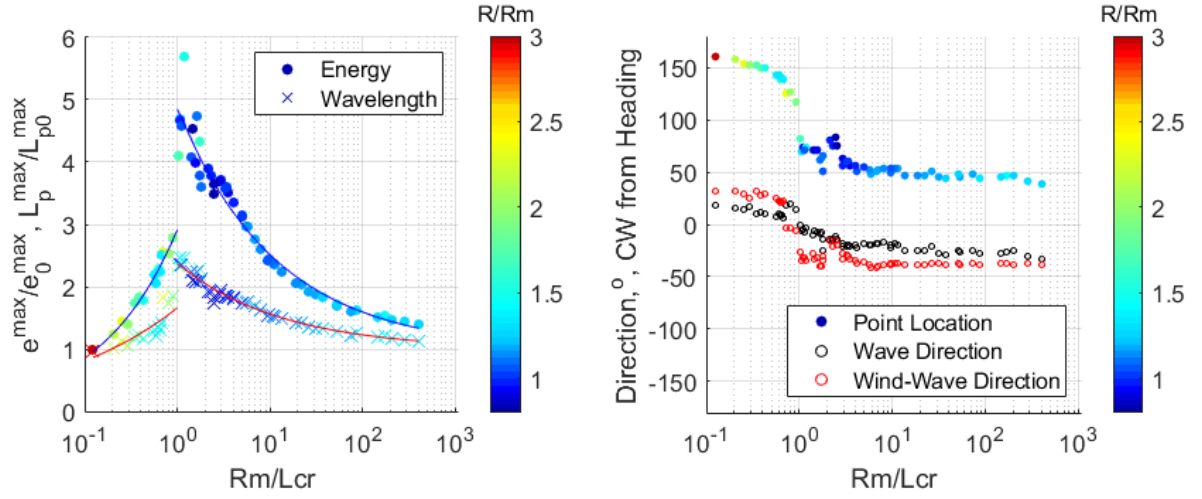
Figure 15. Left: maximal values of the energy (circles) and co-located wavelength (crosses) scaled by the reference values (for stationary TC) as a function of $\tilde{R}_m / \tilde{L}_{cr}^m$ with $\tilde{L}_{cr}^m$ defined by (16). Right: azimuth of position of max energy in TC (filled color circles), direction of the spectral peak (black open circles) and the peak direction relative to the wind one (red open circles) as function of $\tilde{R}_m / \tilde{L}_{cr}^m$. Radial position of max energy and wave direction are shown by color with corresponding color-bar. Solid lines are fits, Eq. (17).
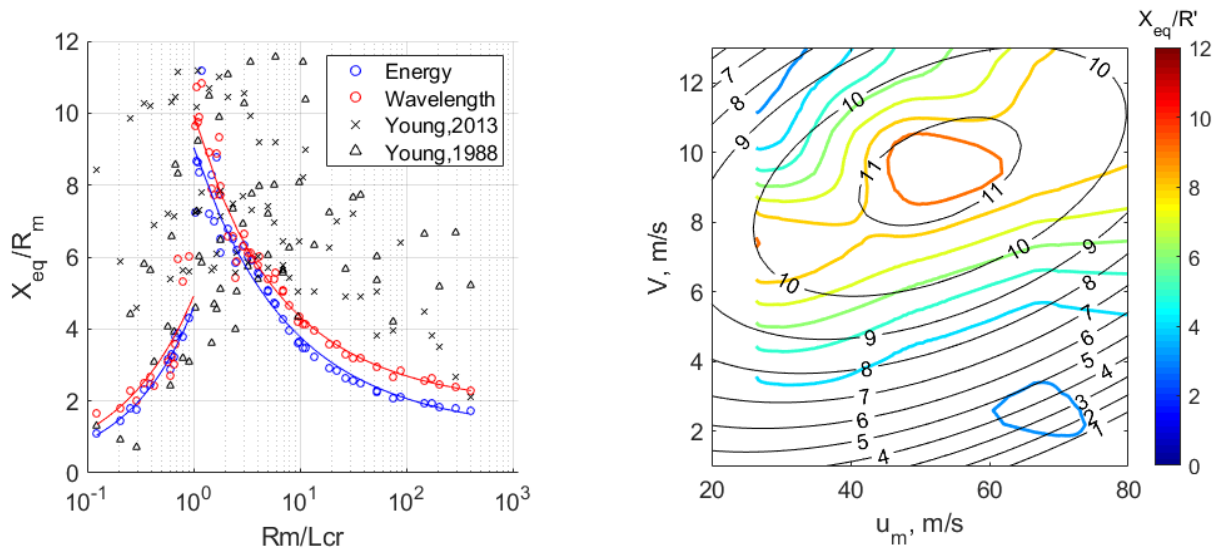
Figure 16. Left: comparison of (open red and blue circles) the model equivalent fetch (6.7) with empirical one suggested by (crosses) Young [1988; relation (6)-(7)] and (triangles) by Young and Vinoth [2013] calculated for 63 TCs used in this study. Right: (color lines) the model equivalent fetch (6.7) and (black lines with numbers) empirical one [Young and Vinoth, 2013, Fig.6b] as a function of maximal wind speed and translation velocity. The fetch is scaled by R' given in [Young and Vinoth, 2013, relation (4)], which is a logarithmic function of Rm.
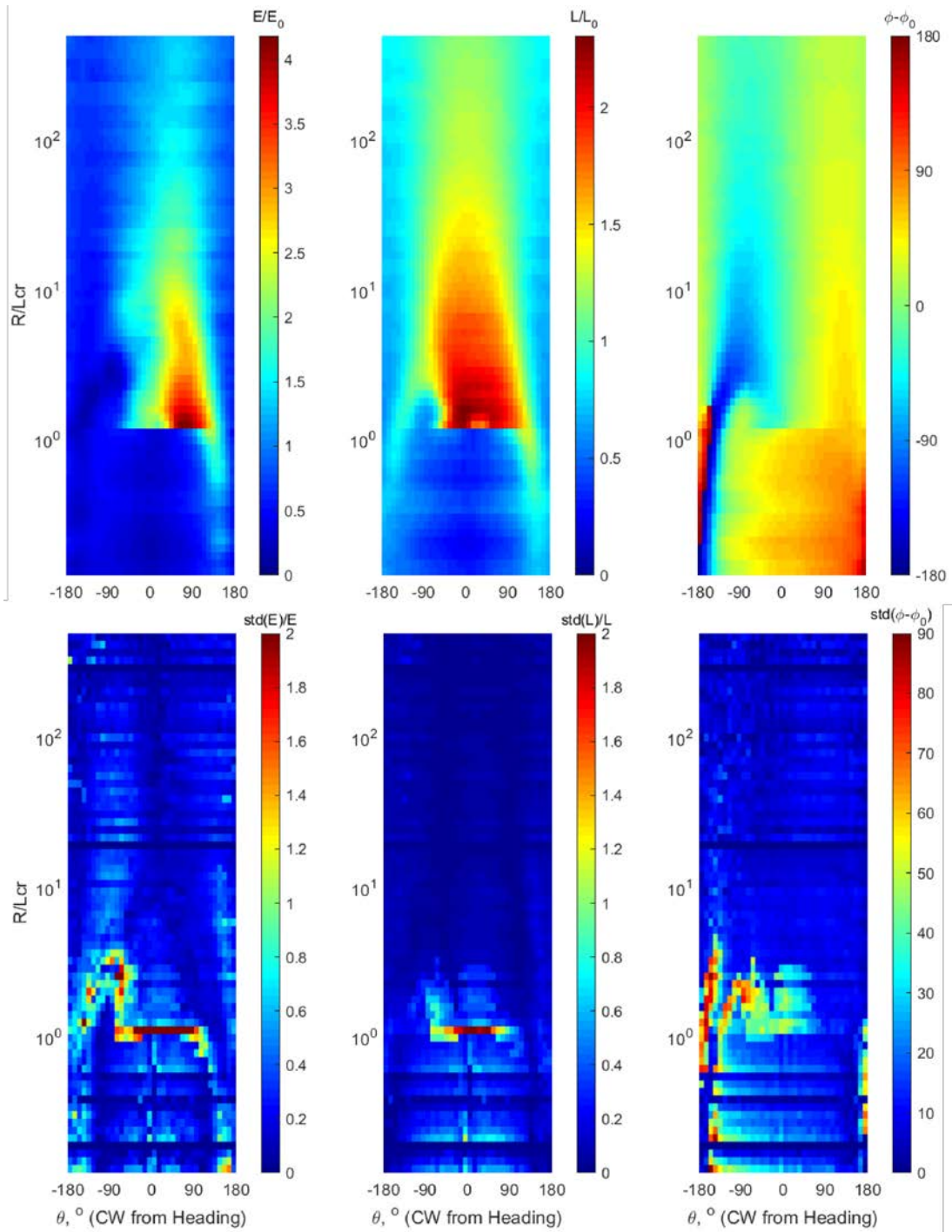
Figure.17. (Upper rows) 2D universal functions (left) $\Phi_e\left(\tilde{r}/\tilde{L}_{cr},\varphi\right)$ for SWH, (mid) $\Phi_\lambda\left(\tilde{r}/\tilde{L}_{cr},\varphi\right)$ for wavelength and (right) $\Phi_\varphi\left(\tilde{r}/\tilde{L}_{cr},\varphi\right)$ for the peak direction in self-similar solutions (7). (Lower rows) Standard deviations of the corresponding functions Φ_e, Φ_λ, and Φ_φ from the mean values shown in the upper rows.
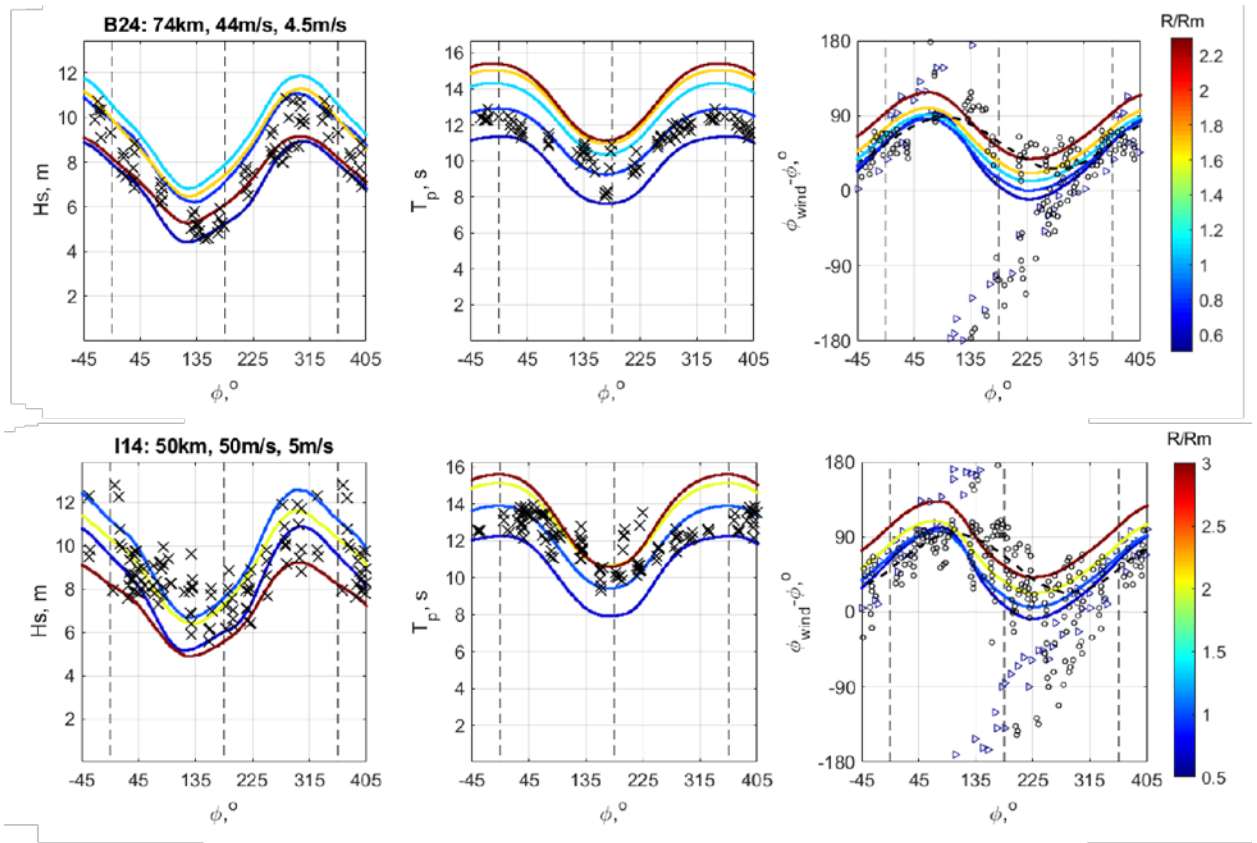
Figure 18. Azimuthal variations of (left) SWH, (mid) peak wave period, and (right) wave direction relative to wind one of primary wave system generated by TCs (upper) Bony and (lower) Ivan. Crosses in the left and mid plots are measurements taken from Hwang and Fan [2017, their Fig 13, cases B24 and I14] for radial distances from $0.5< r/R_m <2.3$ (TC Bony) and $0.5< r/R_m <4$ (TC Ivan). Open circles in the right plots are the measured directions of waves for radial distances taken from Hwang et al. [2017, their Fig.8]; dashed line indicate fit of the data suggested in [Hwang et al., 2017]. Azimuths count from TC heading counter-clockwise. Color lines in all of the plots are self-similar solutions (7) with dimensionless functions shown in Fig.17 for different radial distances, indicated in colorbar. Open triangles in the right plot are numerical model solutions for $r/R_m <0.3$. Parameters of TCs (u_m, R_m, V) used for model simulations are: (74km, 44m/s, 4.5m/s) for Bony and (50km, 50m/s, 5m/s) for Ivan.
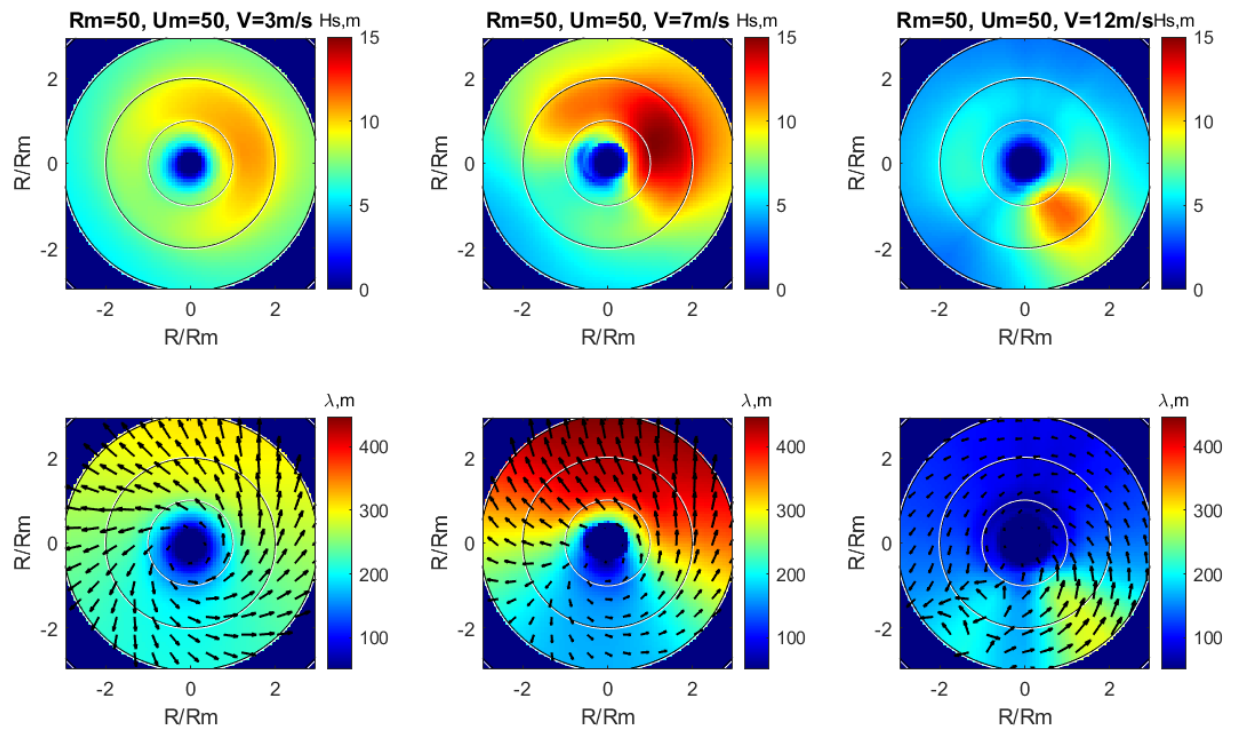
Figure 19. Reconstruction of (upper row) SWH and (lower row) peak wavelength and direction of waves generated by TC with R_m=50km, u_m=50m/s and different translation velocities (3m/s, 7m/s and 12m/s, columns from left-to-right correspondingly). Reconstruction is performed using self-similar solutions (7) with universal functions shown in Fig.17